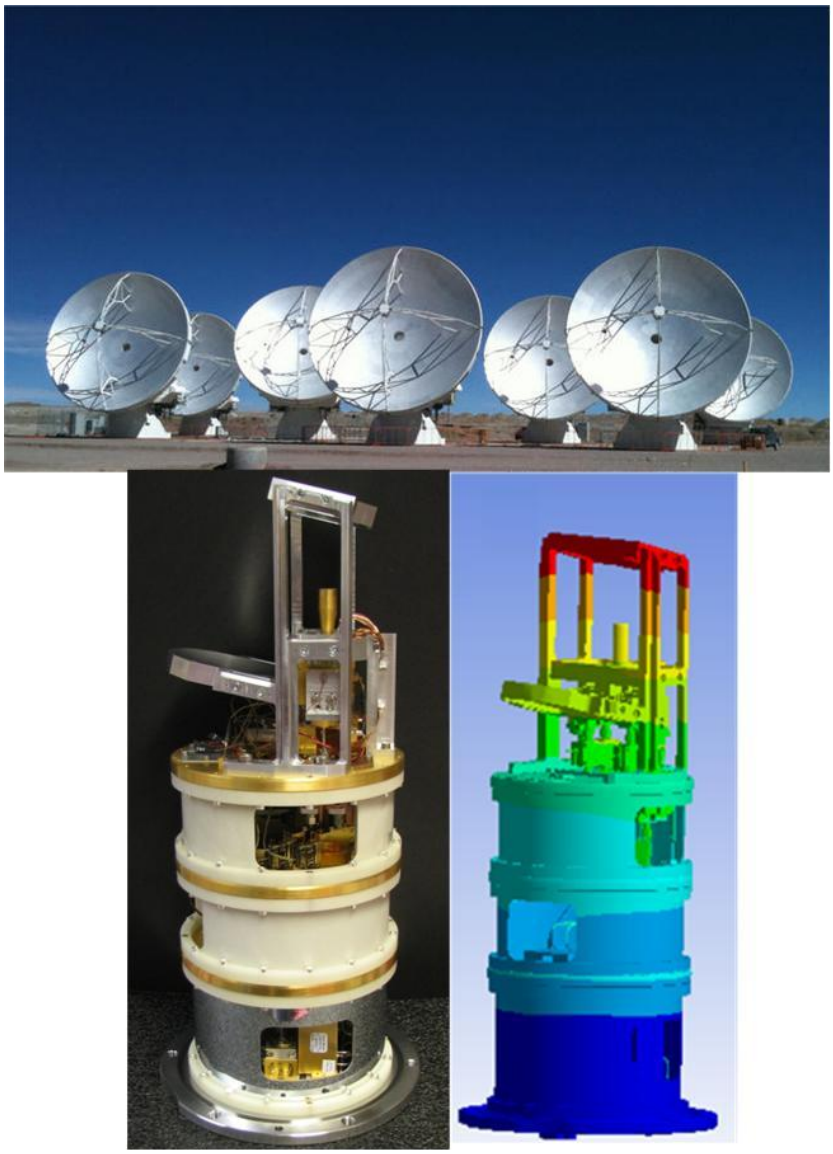

Analysis, Simulation and Cryogenic/Mechanical Design for ALMA Band 5 Cartridge

Magnus Strandberg

Department for Earth and Space Sciences
CHALMERS UNIVERSITY OF TECHNOLOGY
Göteborg, Sweden 2011

THESIS FOR THE DEGREE OF LICENTIATE OF ENGINEERING

Analysis, Simulation and Cryogenic/Mechanical Design for ALMA Band 5 Cartridge

Magnus Strandberg

Technical Report No. 2011: 46L

Group for Advanced Receiver Development
Department of Earth and Space Sciences

CHALMERS UNIVERSITY OF TECHNOLOGY
Göteborg, Sweden 2011

Analysis, Simulation and Cryogenic/Mechanical Design for
ALMA Band 5 Cartridge
MAGNUS STRANDBERG

Technical Report No. 46L
Department of Earth and Space Sciences
Group for Advanced Receiver Development,
Chalmers University of Technology
SE-412 96 Göteborg, Sweden
Telephone + 46 (0)31 772 1000
Fax: +46 (0)31 772 1801
Email: magnus.strandberg@chalmers.se

Cover: The telescopes in the picture are seven ALMA antennas at Chajnantor site, Atacama, Chile. **Credit**: ALMA (ESO/NAOJ/NRAO), Lutz Stenvers (Vertex). At the bottom left a fully eqiuped ALMA Band 5 cartridge is shown. At the bottom left a simulation with ANSYS of the thermal deformation for the ALMA Band 5 cartridge is shown.
.

Printed by Chalmers Reproservice
Chalmers University of Technology
SE_41296 Göteborg, Sweden

Göteborg, Sweden 2011

Analysis, Simulation and Cryogenic/Mechanical Design for
ALMA Band 5 Cartridge
MAGNUS STRANDBERG
Department of Earth and Space Sciences
Chalmers University of Technology

Abstract

This licentiate thesis describes the work conducted by the author during the development of the ALMA Band 5 cartridge. The ALMA project as an international collaboration between various continents consisting of 66 antennas in total with ten ALMA receivers that observes in the range from 31 GHz and 950 GHz. The ALMA Band 5 receiver cartridge is designed for a frequency range of 163-211 GHz.
For achieving the lowest possible system noise temperature, internal key components in the ALMA Band 5 cartridge, such as mixers and amplifiers, should experience a low temperature in the cryogenic region. By optimizing thermal heat load at various temperature stages and create a rigid structure by using various properties of material's behaviour in cryogenic temperature, the cartridge are shown to be fulfilling all specified specifications.

Index Terms – ALMA frontend, receiver cartridge, cryogenics, mechanical stress, thermal contraction.

List of Publications

Appended papers

The thesis is based on the work in the following papers:

Paper A

M. Strandberg, I. Lapkin, V. Belitsky, A. Pavolotsky and S.-E. Ferm, "Analysis, Simulation and Design of Cryogenic Systems for ALMA Band 5 Prototype Cartridge.", *Proceedings of the 20th International Symposium on Space Terahertz Technology*, Charlottesville, April 20-22, 2009, pp. 307-310

Paper B

M. Strandberg, I. Lapkin, "Cryogenic, Mechanical Analysis and Simulation for ALMA Band 5 Prototype Cartridge.", Submitted to Instruments and Experimental Techniques (Pribory i Tekhnika Eksperimenta), 2011

Related papers

Following papers are not included due to overlap with appended papers or outside the scope of the thesis:

Paper C

V. Belitsky, B. Billade, V. Desmaris, D. Dochev, M. Fredrixon, S.-E. Ferm, G. Johnsen, I. Lapkin, D. Meledin, O. Nyström, A. Pavolotsky, H Rashid, E. Sundin, **M. Strandberg**, "Design and performance of ALMA band 5 receiver cartridge.", *35th International Conference on Infrared Millimeter and Terahertz Waves (IRMMW-THz)*, Sept. 5-10 2010

Paper D

V. Belitsky, B. Billade, V. Desmaris, D. Dochev, M. Fredrixon, S.-E. Ferm, G. Johnsen, I. Lapkin, D. Meledin, O. Nyström, A. Pavolotsky, H. Rashid, E. Sundin, **M. Strandberg**, "Advanced Technologies for Radio Astronomy Instrumentation.", *Osservatorio Astronomico di Roma*, 2010

Paper E

B. Billade, I. Lapkin, O. Nyström, E. Sundin, M. Fredrixon, **M. Strandberg**, D. Meledin, S.-E. Ferm, H. Rashid, V. Desmaris, D. Dochev, G. Johnsen, A. Pavolotsky, V. Belitsky, "Design and Performance of ALMA Band 5 Receiver Components.", *Osservatorio Astronomico di Roma*, 2010

Paper F

O. Nyström, I. Lapkin, V. Desmaris, D. Dochev, S.-E. Ferm, M. Fredrixon, D. Henke; D. Meledin; R. Monje, **M. Strandberg**, E. Sundin, V. Vassilev, Victor Belitsky, "Integrated

Setup for THz Receiver Characterization.", *Proceedings of The 21st International Symposium on Space Terahertz Technology,* 23-25 March 2010. Oxford.

Paper G

V. Belitsky, I. Lapkin, B. Billade, E. Sundin, A. Pavolotsky, D. Meledin, V. Desmaris, **M. Strandberg**, R. Finger, O. Nyström, M. Fredrixon, S.-E. Ferm, D. Dochev, H Rashid, D. Henke, "Prototype ALMA Band 5 Cartridge: Design and Performance.", *Proceedings of the 20th International Symposium on Space Terahertz Technology*. April 20-22, 2009. Charlottesville.

Paper H

V. Belitsky, B. Billade, V. Desmaris, D. Dochev, S.-E. Ferm, M. Fredrixon, G. Johnsen, I. Lapkin, D. Meledin, O. Nyström, A. Pavolotsky, H Rashid, **M. Strandberg**, E. Sundin, R. Monje, C. Risacher, D. Henke, V. Vassilev, "Terahertz Instrumentation For Radio Astronomy.", *International Symposium on Terahertz Science and Technology between Japan and Sweden*. November 18-20, 2009, Göteborg, Sweden.

Paper I

D. Meledin, A. Pavolotsky, V. Desmaris, I. Lapkin , C. Risacher, V.P. Robles, D. Henke, O. Nyström, E. Sundin, D. Dochev, M. Pantaleev, M. Fredrixon, **M. Strandberg**, B. Voronov, G. Goltsman, V. Belitsky, "1.3-THz Balanced Waveguide HEB Mixer for the APEX Telescope.", *IEEE TRANSACTIONS ON MICROWAVE THEORY AND TECHNIQUES*, 57 (1) pp. 89-98

Paper J

O. Nyström, I. Lapkin, V. Desmaris, D. Dochev, S.-E. Ferm,; M. Fredrixon, D. Henke, D. Meledin, R. Monje, **M. Strandberg**, E. Sundin, V. Vassilev, V. Belitsky, "Optics Design and Verification for the APEX Swedish Heterodyne Facility Instrument (SHeFI).", *Journal of Infrared, Millimeter and Terahertz Waves*, 30 (7) pp. 746-761.

Paper K

I. Lapkin, O. Nyström, V. Desmaris, D. Meledin, D. Dochev, V. Vassilev, **M. Strandberg**, R. Monje, D. Henke, E. Sundin, S.-E. Ferm, M. Fredrixon, V. Belitsky, "Optics Design and Verification for the APEX Swedish Heterodyne Facility Instrument (SHeFI).", *Proceedings of The 19th International Symposium on Space Terahertz Technology, Groningen, 28-30 April, 2008, ed. W. Wild, Space Research Organization of the Netherlands (SRON)* , Part I pp. 351-357.

Paper L

D. Meledin, V Desmaris, S.-E. Ferm, M Fredrixon, D. Henke, I. Lapkin, O. Nyström, M. Pantaleev, A. Pavolotsky, **M. Strandberg**, E. Sundin, V. Belitsky, "APEX Band T2: A 1.25 – 1.39 THz Waveguide Balanced HEB Receiver.", *In Proceedings of The 19th International Symposium on Space Terahertz Technology, Groningen, 28-30 April, 2008, ed. W. Wild, Space Research Organization of the Netherlands (SRON)* , part I pp. 181-185.

Paper M

V. Vassilev, D. Meledin, I. Lapkin, V. Belitsky, O. Nyström, D. Henke, A. Pavolotsky, R. Monje, C. Risacher, M. Olberg, **M. Strandberg**, E. Sundin, M. Fredrixon, S.-E. Ferm, V. Desmaris, D. Dochev, M. Pantaleev, P. Bergman, H. Olofsson, "A Swedish heterodyne facility instrument for the APEX telescope." *Astronomy & Astrophysics*, 490 (3) pp. 1157-1163.

Paper N

V. Belitsky, I. Lapkin, V. Vassilev, R. Monje, A. Pavolotsky, D. Meledin, D. Henke, O. Nyström, V. Desmaris, C. Risacher, **M. Svensson***, M. Olberg, E. Sundin, M. Fredrixon, D. Dochev, S.-E. Ferm, H. Olofsson, "Facility Heterodyne Receiver for the Atacama Pathfinder Experiment Telescope.", *Proceedings of Joint 32nd International Conference on Infrared Millimeter Waves and 15th International conference on Terahertz Electronics, Sept 3-7, 2007, City Hall, Cardiff, Wales, UK*, pp. 326-328. ISBN/ISSN: 1424414303

Paper O

C. Risacher, V. Belitsky, I. Lapkin, R. Monje, M. Pantaleev, V. Vassilev, E. Sundin, A. Pavolotsky, D. Meledin, K.-Å. Johansson, L.-G. Gunnarsson, **M. Svensson***, M. Fredrixon, S.-E. Ferm, V.P. Robles, M. Hagström, R. Booth, "A 279-381 GHz SIS Receiver for the APEX Telescope.", *Proceedings of the 16th International Symposium on Space Terahertz Technology, Chalmers University of Technology, Gothenburg, Sweden, May 2-4, 2005*, pp. 432-437.

Paper P

C. Risacher,V. Vassilev, R. Monje, I. Lapkin, V. Belitsky, A. Pavolotsky, M. Pantaleev, P. Bergman, S.-E. Ferm, E. Sundin, **M. Svensson***, M. Fredrixon, D. Meledin, L.-G. Gunnarsson, M. Hagström, K.-Å. Johansson, M. Olberg, R. Booth, H. Olofsson, L.-Å. Nyman, "A 0.8 mm heterodyne facility receiver for the APEX telescope.", *Astronomy & Astrophysics*, 454 pp. L17-L20.

Paper Q

M. Pantaleev, V. Belitsky, K. Ermisch, M. Fredrixon, **M. Svensson***, "A Gaussian Beam Measurement Range for mm and Sub-mm Receivers.", *Proceedings of Fifteenth International Symposium on Space Terahertz Technology Massachusetts, USA*, pp. www.stt.2004.org/.

Paper R

M. Pantaleev, K. Ermisch, M. Fredrixon, **M. Svensson***, V. Belitsky, "Measurement Results of Gaussian Beam Verification for HIFI Instrument of Herschel Space Observatory.", *Proceedings of SPIE in Modeling and Systems Engineering for Astronomy*, 5497 pp. 586-595.

*Svensson was my previous surname

Acknowledgements

I would like to show gratitude to my supervisor Professor Victor Belitsky for giving me the chance fulfilling a licentiate thesis in the field of instrumentation of radio astronomy. You have been a great support during this time with your guidance and encouragement. My co-supervisors Alexey Pavolotsky and Igor Lapkin for their support, encouragement and always sharing their unlimited knowledge and expertise in the field of cryogenic design.
Further people at GARD should be acknowledged; there Erik has always been a good friend since Kiruna, Mathias and Sven-Erik being the nicest people in the world, Denis for his Russian mode which is always entertaining, Olle, Bhushan, Hawal, Vincent, Monika and Gert for always providing assistance and help when needed. Former members of GARD such as Raquel, Doug, Dimitar, Miroslav, Vessen, Victor Perez, Karsten, Ricardo and Christophe are acknowledged for the enjoyment being working with you. An extra acknowledgement to the B5 people at GARD which knows how to enjoy a space soap opera.

My parents, my two siblings Catarina and Anders with families and my cousin Lasse with family should be appreciated for being a part in my life.

Finally, I would like to thank my beautiful wife Marie for all support, encouragement and who has bless me with my daughter Saga which is the star in my life

Table of Contents

Chapter 1

Introduction

It was not until early 1930's the pioneer work done by Karl Jansky started the business with radio astronomy, which before had been limited to the usage of optical observations. During this time, Jansky was working at Bell Telephone Laboratories as a radio engineer and with an investigation of sources of electromagnetic waves that was interfering in radio communication. This study showed that signals from space were detected and laid the foundation to ways to investigate the surround sky and object in space [1].

Since radio waves has much lower wavelength than the light waves that the regular, optic astronomy observes, the information due to electromagnetic emissions from objects in space can be observed through the interstellar dust clouds. The signals in the sub-millimetre range will be attenuated in the atmosphere at a certain loss due to water vapour in the air. This favours for observing in the sub-millimetre range to be at satellites or high altitude locations. One example of a satellite mission is the Swedish satellite Odin, which was launched 2001, designed for a two year lifetime but is still fully operational into its 10th year and still delivering data about star formation and ozone layer in the earth atmosphere [2]. Another example of the satellite missions is the Herschel satellite, launched 2009, and is a European Space Agency project with scientific goals regarding the questions of the galaxy evolution and how the stars were formed throughout the history of the universe. It has the largest single mirror ever built for a space telescope and covers a spectral range from the far infrared to sub-millimetre wavelength region (80-670 μm) [3]. The cost for building and launching of satellites is quite large so the development of radio telescopes has been focusing of ground based solutions, such as APEX, the Atacama Pathfinder Experiment [4] or ALMA, the Atacama Large Millimeter/submillimeter Array [5], which both are located at Llano de Chajnantor in the Atacama Desert in Northern Chile, about 5000 meters above sea level. This site has been proved to be a very dry place at a very high altitude, demonstrating exceptionally high transmission of the atmosphere at this place for an average weather with 0.5 mm perceptible water vapour (Figure 1).

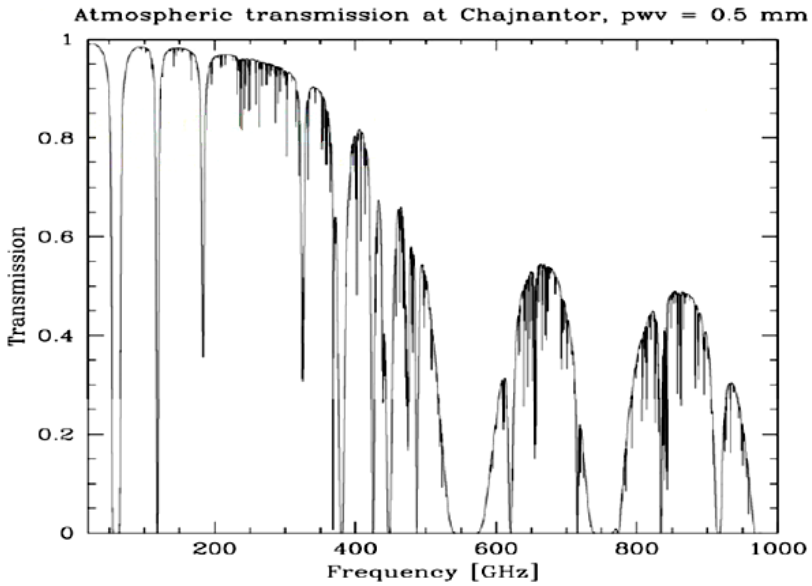

Figure 1. Atmospheric transparency at the, Llano de Chajnantor, with 0.5 mm precipitable water vapor [4].

This thesis concerns the cryogenic and mechanical design of the ALMA Band 5 conducted during development of the prototype for the ALMA Band 5 cartridge. It deals also with development and optimization of internal components, DC wiring length, heat sinks, etc., for fulfilling given specifications for heat load, Eigen frequency, weight limitation and optics.

Chapter 2 gives the outlook of the ALMA project and a description of the ALMA front end. The concept of noise limiting the sensitivity of the system and a brief explanation of superconductivity due to the usage of superconducting materials in cryogenic temperature inside the ALMA Band 5 cartridge are presented.

Chapter 3 presents theoretical grounds of cryogenic engineering with a brief history section to continue with basic definitions such as thermodynamics. Heat transfer and heating mechanism modes are discussed and so also thermal deformation for moving over to properties of materials which plays an important role for design of cryogenic systems. The chapter ends with a presentation of the mechanical properties.

Chapter 4 brings up an analysis section with an extensive presentation of the ALMA Band 5 cartridge and specifics given by the ALMA project. Design issues with internal components are describing with a model for optimizing balance between the conducting heat flux and the heat developed by DC current in DC wires. The work with finding the optimal design of heat sinks is presented. Studies of the thermal contraction of both the cartridge and the optics structure are given. Furthermore mechanical design for fulfilling specification of Eigen frequency and magnetic flux analysis results are provided together with stress analysis for internal cabling.

Chapter 2

Radio Astronomy Instrumentation

2.1. The ALMA Project

The ALMA telescope is an international collaboration between Europe, North America and East Asia in cooperation with the Republic of Chile. It will consist of 54 moveable antennas of 12 meter in diameter and twelve 7-meters diameter antennas with their 10 bands, ALMA receivers will cover the frequency range from 31 GHz to 950 GHz. The ALMA Band 5 receiver cartridge, which is the subject of this thesis, is designed for a frequency range of 163-211 GHz. The ALMA receiver bands are presented in TABLE 1.

TABLE 1. THE FREQUENCY BANDS OF ALMA [5].

ALMA Receiver band	**Frequency range (GHz)**	**Produced by**
1	31-45	tbd
2	67-90	tbd
3	84-116	HIA
4	125-163	NAOJ
5	163-211	OSO
6	211-275	NRAO
7	275-373	IRAM
8	385-500	NAOJ
9	602-720	NOVA
10	787-950	NAOJ

2.1.1. ALMA front end

The ALMA Band 5 receiver cartridge is one of ten cartridges that will occupy the ALMA cryostat in the ALMA telescopes. The cryostat with the cryo-cooler attached is the largest single component of the front end system and will assist the cartridges to reach the operating

temperature of 4 Kelvin. The cryostat has a height of 620 mm diameter of 970 mm and has a three-stage cryo-cooler of nominal temperatures of 4, 15 and 110 Kelvin [6].

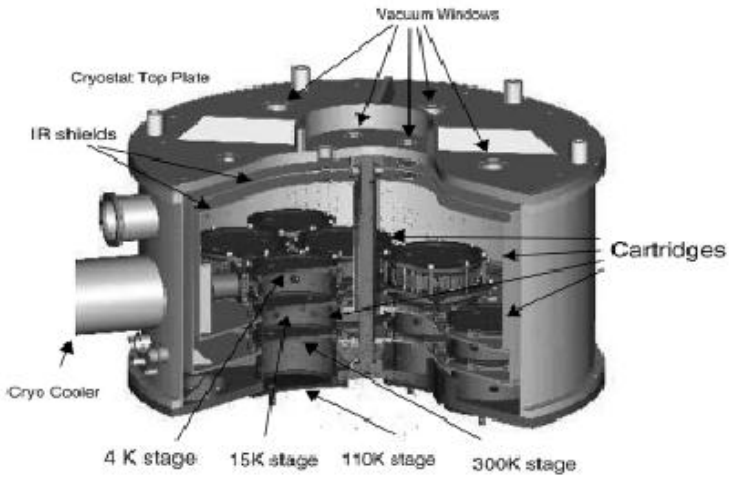

Figure 2. The ALMA cryostat. [6]

The cartridges are all fitting the cylindrical envelope of nominal of 170 mm, except for the cartridges for band 3 and 4, which are 140 mm. All cartridges have same temperature as the cryostat for operation, except band 1 and 2 which does not require reaching 4 K.
An ALMA cartridge has structure of a base plate with a temperature of 300 K and 3 sub-assembly sections of 4 K, 15 K and 110 K, separated by G10 fibreglass for improvement of thermal insulation between the various stages. The stages are made off different materials: the bottom 300 K stage is made of stainless steel; the 110 K stage is made of aluminium, and both 15 K and 4 K stages are made of copper. The G10 tube between the stages of 300 K and 110 K has an extra layer of an aluminized Mylar to shield the excessive heat loading due to radiation [7].

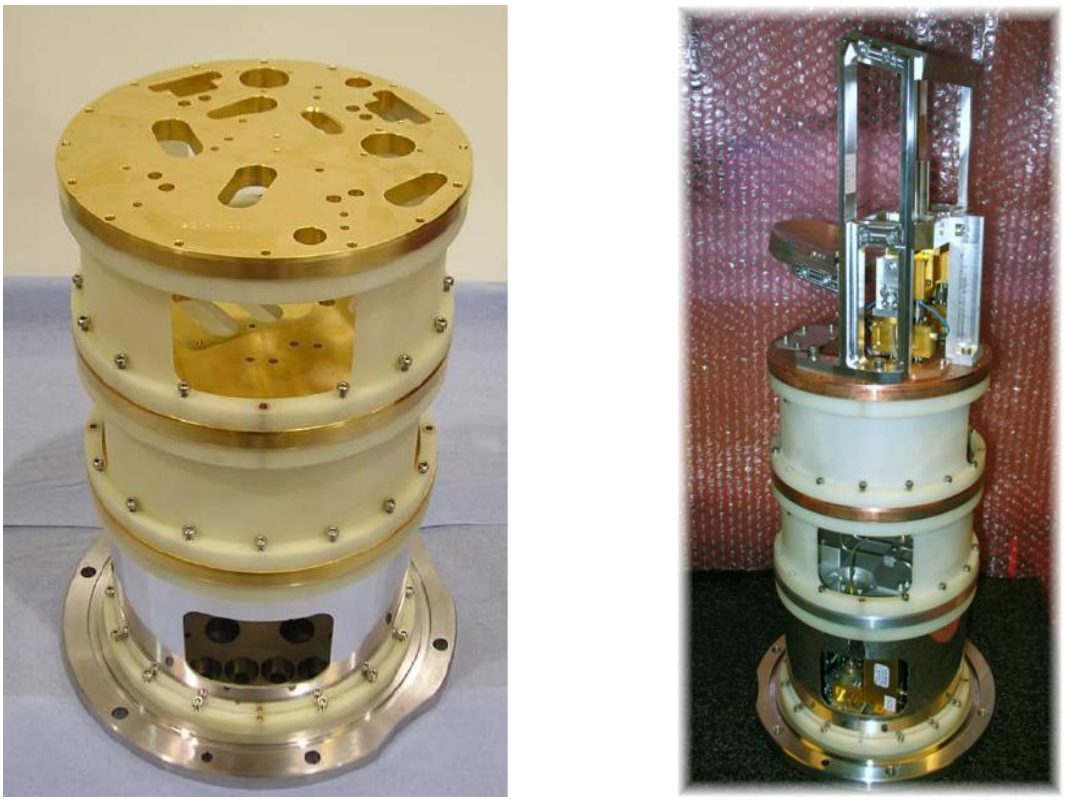

Figure 3. To the left, an ALMA Band 5 cartridge without any receiver part mounted [8]. To the right, a fully equipped ALMA Band 5 cartridge.

The fully equipped ALMA Band 5 receiver cartridge has components, such as mixers, which need cryogenic temperature for operation, as well as amplifiers, which require cryogenic cooling for ultimate noise performance [9].

2.1.2. Thermal Noise and Superconductivity

To reduce the thermal noise, also called Johnson noise, which exist in any component that has a temperature above 0 Kelvin, certain measured has to be taken. The thermal noise is generated by thermally excited electrons so for reducing this phenomenon, materials that are working well in low temperatures are used. The noise power delivered to a matched load is

$$P_n = k_B TB \tag{2.1}$$

where k_B is the Boltzmann's constant, T is the ambient temperature and B is the bandwidth. This shows that the noise is in direct correlation with the bandwidth and the temperature. By setting the amplifiers in the receiver configuration to a cooling temperature of cryogenic region then a weak signal has a better probability of being measurable with lower noise. The noise temperature of the system includes loss in the atmosphere, the antenna with optical losses, and receiver (for heterodyne receiver it is mixer and IF amplifier). Thus the noise temperature of the system becomes:

$$T_{sys} = T_{ant} + T_{rf\_amp} + \frac{T_{mix}}{G_{rf\_amp}} + L_{mix} \cdot \frac{T_{if\_amp}}{G_{rf\_amp}} + L_{mix} \cdot \frac{T_{following}}{G_{rf\_amp} \cdot G_{if\_amp}} \tag{2.2}$$

where T_{ant} is the loss in the atmosphere together with antenna loss and spillover losses. The contribution of the terms G_{rf_amp} and T_{rf_amp} in equation (2.2) is valid for receivers operating from 30 MHz to 100 GHz when a RF low noise amplifiers is used. Over 100 GHz the amplifiers are too noisy and it makes it more preferable to down convert the signal in prior to the amplifier.

For receivers in the region of 100-1000 GHz (as B5CCA is between 163-211 GHz) the most common mixer to use is Superconductor-Insulator-Superconductor (SIS) junction and is described in [10] and [11]. This device consists of two superconductor materials separated by a thin insulator and has a non-linear current-voltage characteristic. This is caused by quasiparticles tunnelling through the isolator.

The material of a superconductors acts like a normal metal above its critical temperature T_c while under has features as zero DC electrical resistance and perfect diamagnetism, also known as Meissner effect [12]. This effect is when a magnetic field can't exist inside the material. The material for the most common SIS junctions is based on Niobium with some variations with a typical T_c around 9 Kelvin [13] hence the receiver requires a temperature in the cryogenic region.

Chapter 3

Elements of Cryogenic Engineering

This thesis deals with thermo-mechanical analysis of the ALMA Band 5 cold cartridge assembly design and its optimization for operation at cryogenic working conditions. This chapter covers some elements of cryogenic and mechanical engineering, giving a basis for Band 5 cartridge design analysis and optimization.

3.1. Theory of Cryogenic Engineering

The term cryogenics refers to the scientific and technology field dealing with low temperatures, often assuming temperature range below 120 Kelvin [14]. Historically, first refrigerating techniques made use of naturally cold objects (ice, snow), cooling by evaporation, or dissolving (for example, sodium or potassium nitrate, saltpetre, dissolving in water) [15]. But a demand for lower temperature caused sufficient progress in refrigerating technology, which opened the possibility to study material behaviour at really low, cryogenic, temperatures.

The first major breakthrough was done when the Joule–Thomson effect was discovered in 1852 [16] and the next one was in the year 1877 when the first liquefaction of oxygen was achieved by the French scientist Cailletet and Picet from Genova which independently presented theirs result. The approach by Cailletet was by using a hand-operated screw jack with mercury to pressurize oxygen to 200 bars to a glass tube cooled down by liquid ethylene of 169 Kelvin. Picet used a cascade of vapour-compression systems for pre-cooling the oxygen, namely a first stage with sulphur dioxide (263 K) and a second stage with carbon dioxide (195 K)[14, 15]. Over the following centuries the methods and equipment for liquefying become better such as Linde and Hampson which in 1895 managed to build air liquefiers with recuperative heat exchanger and in 1898 Dewar manages to liquefy hydrogen [17]. Some years before Dewar in 1892 built the first vacuum insulated storage container, therefore a vacuum chamber is often referred as a *Dewar*. Kamerlingh-Onnes succeeded in 1908 with the liquefaction of helium by using the Joule–Thomson expansion i.e. a gas will change its temperature when it expands slowly through a partially–opened valve, a porous

plug or similar [18]. Only a couple years later, namely in 1911 Kamerlingh-Onnes and his team at Leiden discovered superconductivity [19].

Applications for cryogenics are vast and include things like liquefaction and separation of gases, space technology as satellites, telescope and rockets, food conservation, etc. This list can go on and on.

3.2. Heat Transfer and Heating mechanisms

3.2.1. Heat Transfer

Heat transfer in a system refers the *first* law of thermodynamics and takes the following equation for a closed system:

$$Q = Wk + \frac{dU}{dt} \tag{3.1}$$

where Q is the heat transfer rate, Wk is work transfer rate and the derivate dU/dt is the rate of the change of the internal thermal energy, U, with time, t [20]. This can be written as (3.2):

$$Q = p\frac{dV}{dt} + \frac{dU}{dt} \tag{3.2}$$

with the work done on the environment is a product of pressure (p) and volume (dV) change. In case of constant-volume process, this leads to

$$Q = \frac{dU}{dt} = mc_v \frac{dT}{dt} \tag{3.3}$$

and in case of constant-pressure process:

$$Q = \frac{dH}{dt} = mc_p \frac{dT}{dt} \tag{3.4}$$

Where T is temperature, m is the mass, H is the enthalpy and respectively c_v and c_p are the specific heat capacities at constant volume and constant pressure. If now the process for the material has a constant volume for any pressure variation, c_v and c_p are equal and (3.2) is written

$$Q = \frac{dU}{dt} = mc\frac{dT}{dt} \tag{3.5}$$

If now the system of heat transfer was reversible equation (3.2) would be written as (3.6)

$$T\frac{dS}{dt} = p\frac{dV}{dt} + \frac{dU}{dt} \tag{3.6}$$

with *S* as the entropy. Now heat between two thermal containers with constant temperatures, T_H and T_L will always flow from T_H to T_L, as long $T_H > T_L$. If no temperature difference is occurring then the rate of the heat transfer is zero.

Heat Conduction

The heat transfer due to conduction is present when a temperature gradient exists in a solid, and energy transfers from a region with a higher-temperature to a region of lower-temperature. This is shown in equation (3.7) in 1D case, where the transfer of energy is due to conduction and the transfer rate per area unit is proportional to the normal temperature gradient.

$$Q = -\lambda(T) A \frac{dT}{dx} \tag{3.7}$$

where λ is the thermal conductivity (temperature dependent) of the material, *A* the cross-section area and *dT/dx* is the temperature gradient in the material [21]. If equation (3.7), called the Fourier law for a homogeneous media is expanded for a conductor with length L and between temperatures T_1 and T_2, equation (3.8) is obtained for steady-state conditions:

$$Q = \frac{A}{L} \int_{T_1}^{T_2} \lambda(T) dT \tag{3.8}$$

Radiation

The net exchange between two surfaces due to a radiant energy is one of the modes of heat transfer in a cryogenic system. In contrast to conduction and convection, radiation does not require media to work. By its nature, radiation heat transfer is propagation of electromagnetic waves. In the electromagnetic wave spectrum, thermal radiation can be found between 0.1 to 1000 μm [20] (Figure 4).

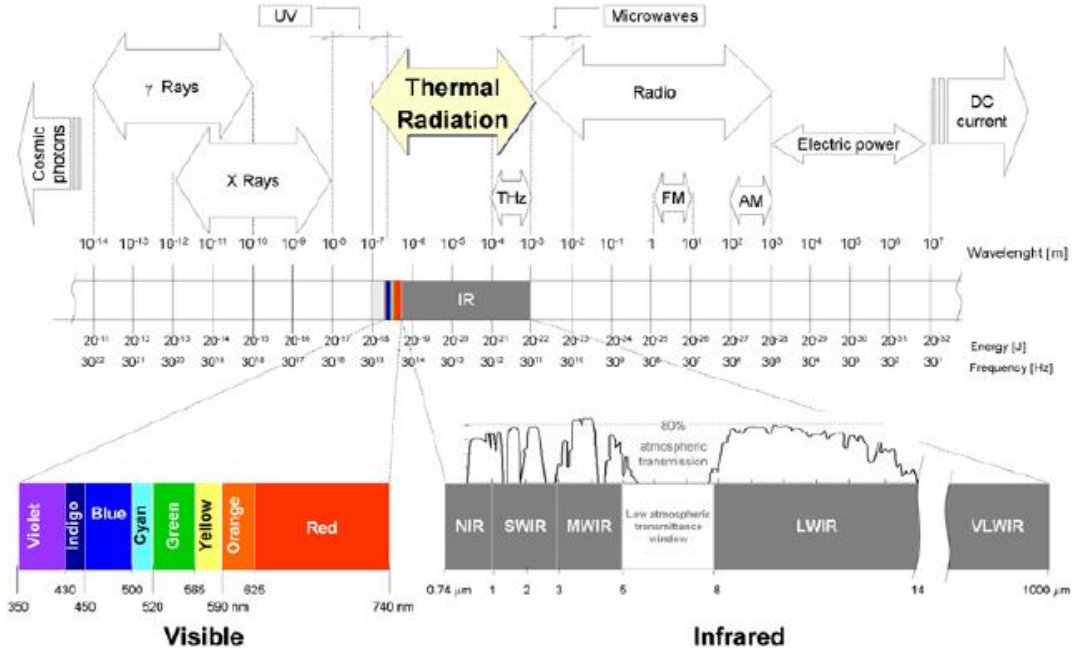

Figure 4. The electromagnetic wave spectrum [22].

Radiated energy is given by Stefan-Boltzmann law [23]

$$E_b = \sigma T^4 \tag{3.9}$$

where E_b is energy radiated by a ideal radiator and σ is the Stefan-Boltzmann constant. Equation (3.9) defines the surface of a black body and represents the maximum amount of heat that can be radiated by a body with a temperature T. This energy is distributed over a range of wavelength as shown in Figure 5 with some temperatures. The radiant energy decreases rapidly with falling temperatures and while wavelength for the maximum energy increases. This wavelength is known by Wien's displacement formula

$$\lambda_{max} T = Const. \tag{3.10}$$

The constant has a value of 2900 μmK.

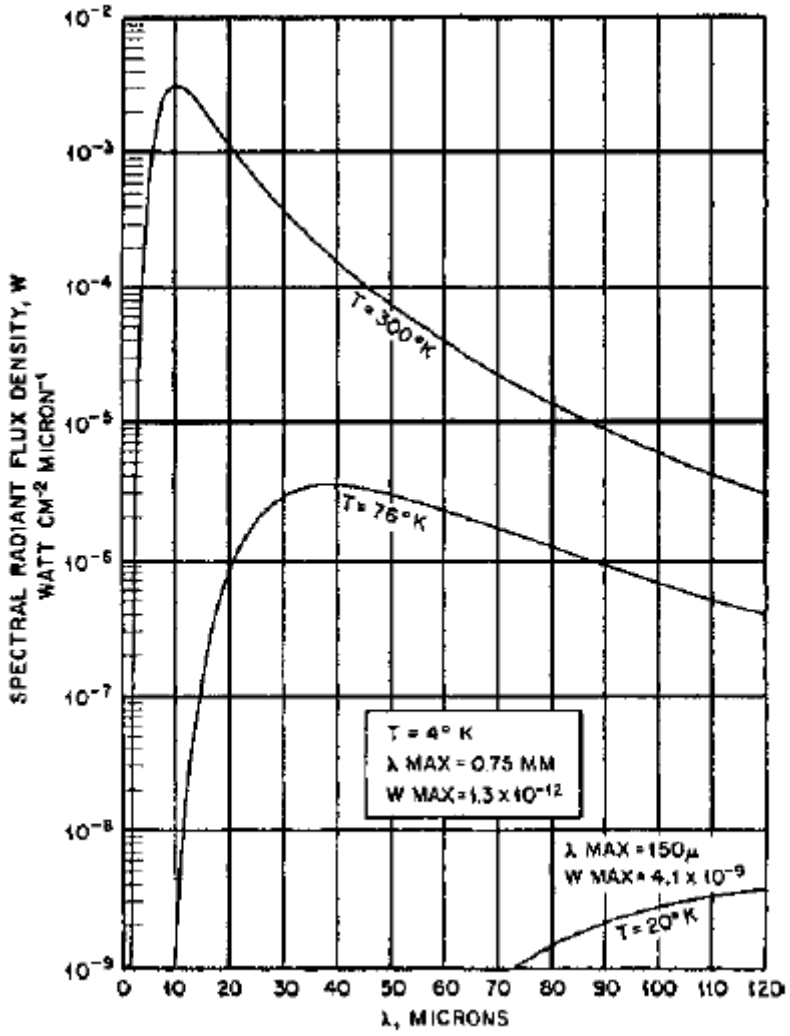

Figure 5. The wavelength energy graph of the black body radiation. [24]

Real, not absolutely black, surface emits and absorb less than follows from Eq. (3.10), depending on angle and wavelength, and also reflect radiation, and also it reflects some of radiation, as described by expression (3.12) for reflectivity ρ, absorptivity α and the transmissivity τ [21].

$$\rho+\alpha+\tau=1 \tag{3.11}$$

When radiation hits a surface, the reflection can be of two types, either *specular* or *diffuse*. When the angle of incidence is the same as the angle of the reflection, reflection is referred as specular. Alternatively, when the incident beam is distributed in all directions, reflection referred as diffuse. Real surfaces are not either pure specular, or diffuse [21]. A surface, like a mirror, that acts like specular for a wavelength range of thermal radiation (visible light) might be diffuse for the rest of the wavelengths. For a polished surface, it demonstrates specular behaviour than diffuse while a rough one shows the reverse.

If a real is placed inside a perfectly black enclosure that emits radiation and is obtaining radiant flux, q_i, it comes to temperature equilibrium with the enclosure.

$$E = q_i \alpha \tag{3.12}$$

If the real body inside enclosure is replaced with a black body and comes to equilibrium with the enclosure:

$$E_b = q_i \cdot 1 \tag{3.13}$$

where the blackbody absorptivity is unity and dividing (3.12) with (3.13) gives

$$\frac{E}{E_b} = \alpha \tag{3.14}$$

This ratio between the emissive power of a body and that of a *blackbody* at the same temperature is equal to the absorptivity of the body, with definition as the emissivity of a body and is called Kirchhoff's identity (3.15).

$$\varepsilon = \alpha \tag{3.15}$$

The emissivity of different materials does vary with wavelength, temperature and the condition of the surface, but for simplification it is common to assume independency of wavelength and direction. This surface is called gray diffuse body and has an emissivity value between 0 and 1.

If two bodies that is separated with a distance *l* in vacuum and has each flat black surfaces at absolute temperatures T_1 and T_2, the radiation heat transfer between these bodies follows the equation (3.16).

$$\frac{Q_R}{A} = E_{b1} - E_{b2} \tag{3.16}$$

Combining (3.10) and (3.16),

$$\frac{Q_R}{A} = \sigma(T_1^4 - T_2^4) \tag{3.17}$$

Account for the surface areas, geometry of the surfaces and the position in relation to each other is given through introducing a *shape factor* or *view factor*, $F_{1\text{-}2}$, what the first object "sees" the other object

$$Q_R = \sigma A_1 F_{1-2}(T_1^4 - T_2^4) \tag{3.18}$$

TABLE 2 shows the view factors for some geometries and individual emissivities for gray surfaces. More view factors can be found in [25]

TABLE 2.VIEW FACTORS FOR VARIOUS GEOMETRIES. A1 AND A2 ARE THE RESPECTIVE AREAS OF SURFACES [19].

Geometry	**Specular reflection**	**Diffuse reflection**
Parallel plates	$\frac{\varepsilon_1\varepsilon_2}{\varepsilon_2+(1-\varepsilon_2)\varepsilon_1}$	$\frac{\varepsilon_1\varepsilon_2}{\varepsilon_2+(1-\varepsilon_2)\varepsilon_1}$
Long coaxial cylinders (L»r)	$\frac{\varepsilon_1\varepsilon_2}{\varepsilon_2+(1-\varepsilon_2)\varepsilon_1}$	$\frac{\varepsilon_1\varepsilon_2}{\varepsilon_2+\frac{A_1}{A_2}(1-\varepsilon_2)\varepsilon_1}$
Concentric spheres	$\frac{\varepsilon_1\varepsilon_2}{\varepsilon_2+(1-\varepsilon_2)\varepsilon_1}$	$\frac{\varepsilon_1\varepsilon_2}{\varepsilon_2+\frac{A_1}{A_2}(1-\varepsilon_2)\varepsilon_1}$

Convection

Thermal convection is a general term for heat transfer through a motion of fluid or gas particles. There are two causes for a convection heat transfer, namely force convection and free convection. Forced convection takes place, when some external force, like a fan or a pump causes fluid or gas motion between surfaces exchanging with heat. Free convection is caused by fluid or gas motion due to temperature induced density difference in it [22, 24].
This leads to the basic equation for Newton's law of cooling in their steady-state form [22]

$$q = hA\Delta T \tag{3.19}$$

Where h is the heat transfer coefficient, A is the surface area where convection takes place and ΔT is the temperature difference.

3.2.2. Heating Mechanisms

Joule Heating

Currents through wires used inside a Dewar / Cartridge cause dissipation of heat:

$$P = RI^2 \tag{3.20}$$

where R is wire resistance and I is current through the wire. It is worth mentioning here that in practice, different fragments of the wire can be at different temperature, so resistance R in the formula above appears to be dependent on temperature and position of the certain fragment of wire.
In chapter 4 of this thesis, an analysis and discussion is presented concerning optimizing of the length for cryogenic wires between 15 K and 4 K temperature stages of the ALMA Band 5 receiver cartridge, accounting for temperature dependence of the wire electrical resistivity and its thermal conductivity.

3.3. Thermal Deformation

Materials exposed to cooling experience contraction (shrinking) due to less thermal vibration of the atoms in the material and hence to a decrease in the average separation distance of the adjacent atoms [26]. The expansion behaviour exists due to the unsymmetrical intermolecular potential energy curve, as shown in Figure 6. This phenomenon is typical of substances except some artificially created materials, having zero or negative thermal-expansion coefficients [27].

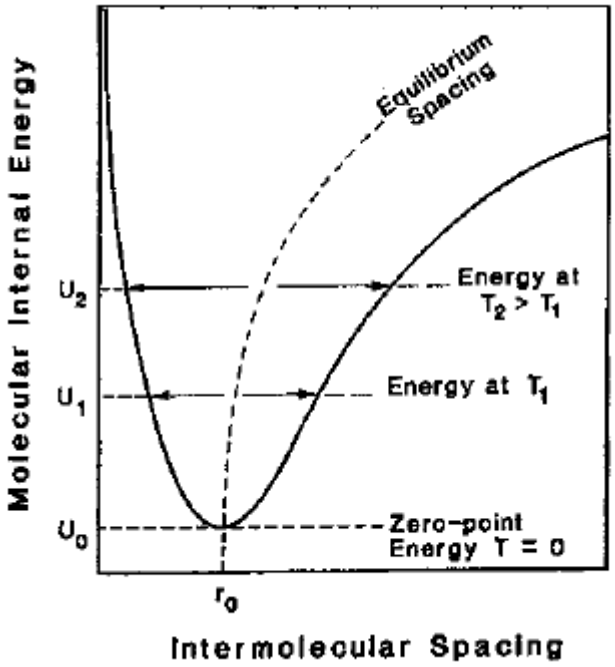

Figure 6. The unsymmetrical intermolecular potential energy curve [24].

Thermal contraction of a material during cooling is described by equation (3.21).

$$d = L\int_{T_1}^{T_2}\alpha(T)\cdot dT \tag{3.21}$$

where L is the linear dimension of the object and α is the instantaneous coefficient of the thermal expansion (contraction), often referred as *CTE*. This coefficient is explained in more details in the section on thermal expansion/contraction coefficient 3.4.4.

The thermal contraction must be taken into account when the internal components in a vacuum chamber is designed and placed. Since different materials have various CTE and hence non-similar contraction, close components must have clearances between them. Otherwise, contraction can cause significant stress in assembly.

3.4. Properties of Materials

For an appropriate design of a cryogenic system knowledge of the properties and behavior of materials are crucial. The properties of a material are often temperature dependent and significantly different compared to that at 20° C, at which those properties are usually referred.
Number of books and websites give experimental data of the properties in the cryogenic region are [14, 18, 19, 24, 28-31].
As a general rule (with some exceptions) the following materials are recommended to use in a cryogenic setting [32].

- The 300 series austenitic steel (particularly the stainless steels 304LN and 316LN for their high mechanical strength and low magnetic permeability).
- OFHC copper.
- Austenitic alloys (in particular Fe-Ni-Cr-N and Fe-Mn-Cr-N alloys and Inconel 908).
- Aluminium alloys (6061, 6063, 1100).
- Titanium and its alloys.
- Niobium.
- Invar.
- Plastics (Kapton, Teflon, cryogenic epoxies).
- Quartz.

Materials not recommended are

- Martensitic steels.
- Quenched or precipitate-aged materials.

3.4.1. Thermal Conductivity

As mention in section *Heat Conduction* the property thermal conductivity is appearing in Fourier's law for heat conduction and is describing the materials ability to conduct heat.

3.4.1.1. Thermal Conductivity in Insulators

In dielectrics the contribution to the energy transfer is by phonon conduction so the quantized vibrational modes are treated as quasi-particles. These phonons collide with each others which can be seen as an analogous to molecules in a gas. Because of that, thermally excited solid can be treated as a gas full of phonons. Equation (3.22) defines the expression for thermal conductivity in insulator [24]

$$\lambda_{insulator} = \frac{C_V U L}{3} \tag{3.22}$$

where C_V is the specific heat of the phonons (or the lattice specific heat); U is the velocity of propagation of the phonons at the speed of sound and L is the mean free path of the phonon between collisions. The '1/3' is due free random movement of the phonons in all directions.

All parts of (3.24) have temperature dependence as seen in Figure 7. The thermal conductivity $\lambda_{insulator}$ is plotted at Figure 7a, the specific heat C_V at Figure 7b, the mean phonon velocity U at Figure 7c, and Figure 7d is the mean free path of the phonon between collisions L.

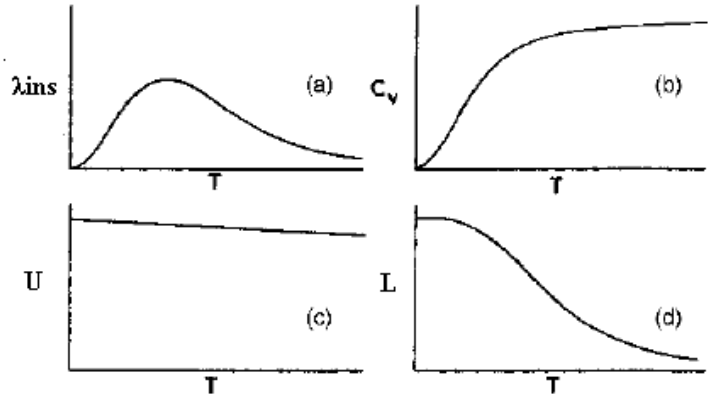

Figure 7. The mechanism behind thermal conductivity of insulators vs temperature. Based on a figure from [24].

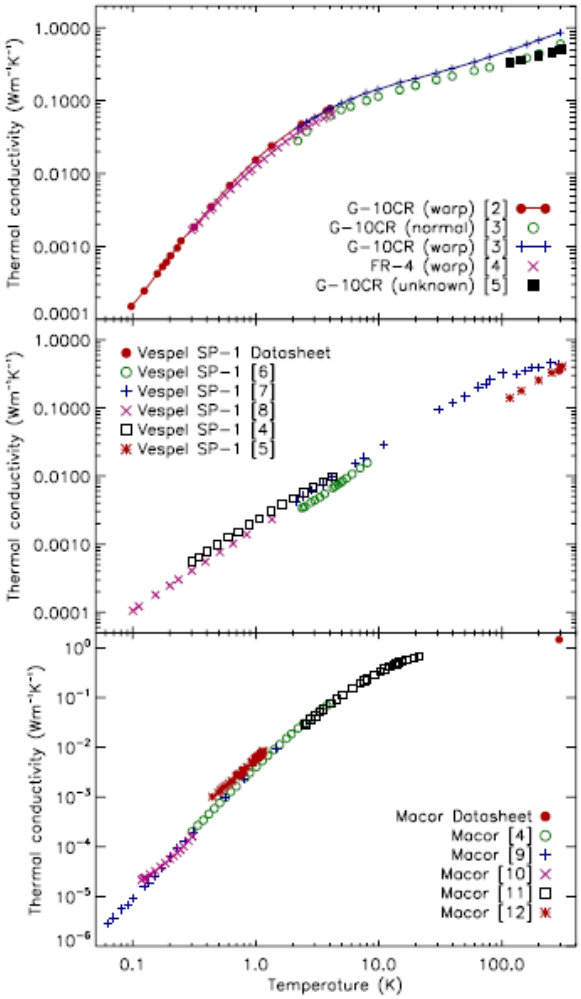

Figure 8. Thermal conductivity of various insulators such as G10CR, G10, FR4, Vespel SP-1 and Macor. The values are from multiple sources and is presented in [33].

Figure 8 and Figure 9 shows summarize the data on thermal conductivity for insulator material commonly used in cryogenic vacuum systems, where G10 is a fibreglass epoxy, the CR mark after is 'cryogenic grade', same as FR4. Vespel SP-1 is an unfilled polyimide material from DuPont used in low cryogenic. Macor is a machinable glass-ceramic with a low thermal conductivity around 10 mK.

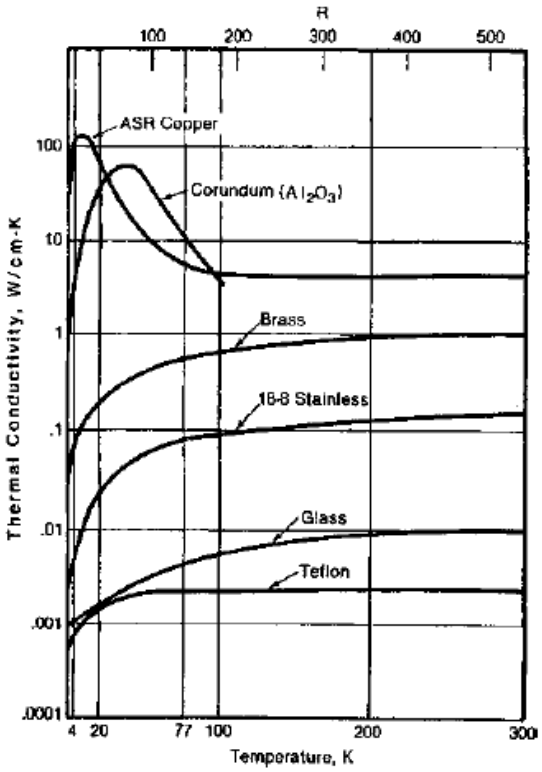

Figure 9. Thermal conductivity of several materials [24].

3.4.1.2. Thermal Conductivity in Metals

The thermal energy in metals is conducted by phonons in the lattice and also by free electrons. The total thermal conductivity λ_t is [24]

$$\lambda_t = \lambda_e + \lambda_p \tag{3.23}$$

where λ_e is the free electron thermal conductivity and λ_p is the quantized lattice vibrations phonons thermal conductivity.
The free electrons conductivity λ_e contributes more to the heat transport than the phonons. This can be defined by equation (3.24), which is an analogue to the equation (3.22) [24]

$$\lambda_e = \frac{C_e U_e L_e}{3} \tag{3.24}$$

Where C_e is the electronic heat capacity, U_e is the mean velocity of the electron and L_e is the mean free path of electrons between collisions. C_e is very small, however U_e is quite big. Also the phonons is scattered by the electrons. All this leads to λ_e is much greater than λ_p for most

pure metals. Because of that, λ_p can be neglected and the total thermal conductivity becomes [24]

$$\lambda_t = \frac{C_V' UL}{3} \tag{3.25}$$

As seen in Figure 10a, the thermal conductivity λ_t varies with temperature as such as the terms. The specific heat C'_v has a constant together the temperature (b) while the electron velocity U is independent of the temperature (c). As seen in (d) the mean path varies with temperature in the same way for phonons.

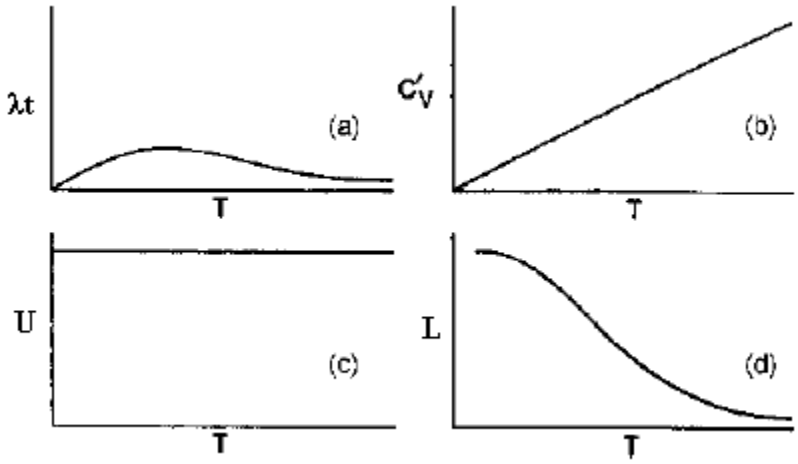

Figure 10. The thermal conductivity mechanism vs temperature of metals. Based on a figure from [24]

The data on thermal conductivity of several solids is summarized on Figure 11, Figure 12 and Figure 13.

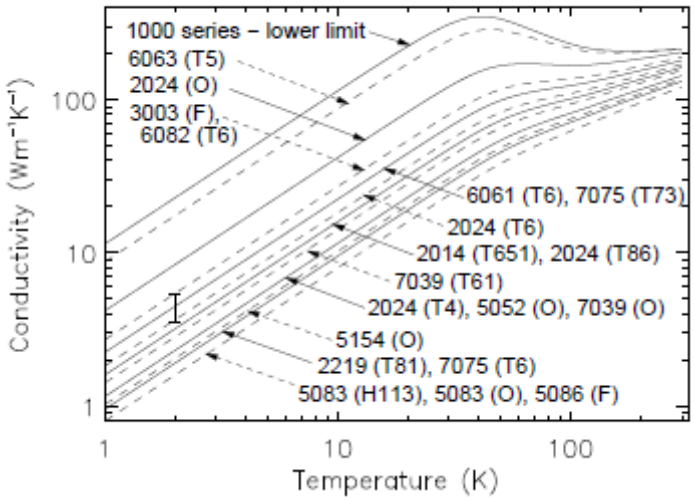

Figure 11. Thermal conductivities for aluminium alloys and from multiple sources as shown in [34]

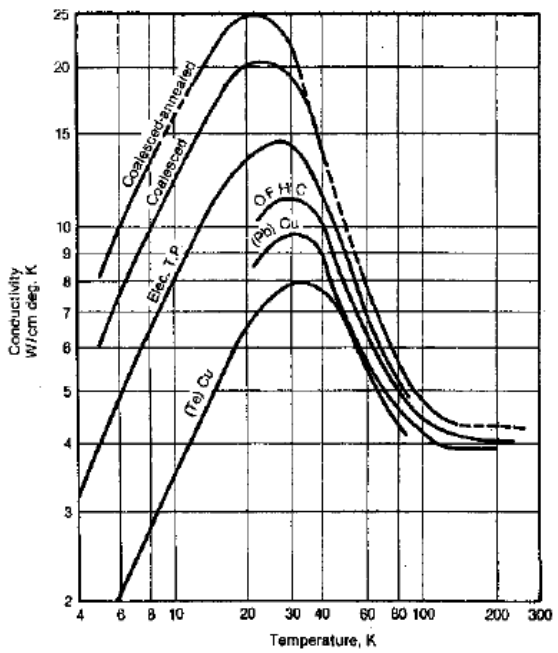

Figure 12. Thermal conductivity of copper of different types [24].

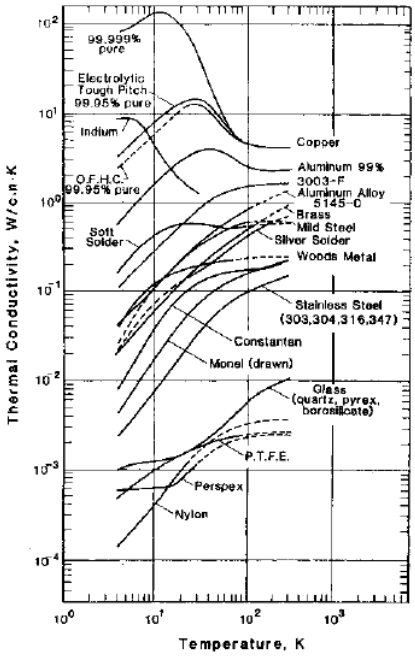

Figure 13. Thermal conductivity of various materials [24].

According to the figures above, metal of high purities exhibit a maximum thermal conductivity at low temperatures which in many cases are several times higher than at room temperature.

A phenomenological model for determining the thermal conductivity in superconductors was developed by Callaway. The model does aid calculation for phonon scattering process in lattice [35].

$$\lambda = CT^3 \int_0^{\vartheta_D/T} \frac{x^4 e^x (e^x - 1)^{-2} dx}{\tau^{-1}} \tag{3.26}$$

where

$$C = \left(\frac{k_B}{2\pi^2 v_s} \right) \left(\frac{k_B}{\hbar} \right)^3 \tag{3.27}$$

and

$$x = \frac{\hbar\omega}{k_B T} \tag{3.28}$$

The term k_B as Boltzmann's constant, v_s is the average phonon velocity, $\hbar$ the reduced Plank constant, ω the angular frequency and T is the temperature.
The total inverse relaxation time is [36]

$$\tau^{-1} = (v_s / LF) + A\omega^4 + (B_1 + B_2)\omega^2 T^3 \tag{3.29}$$

The first tem (v_s/LF) is Casimir expression for the boundary scattering with L as the equivalent sample size (i.e. cross section) and F is a geometric factor.
The second term $A\omega^4$ is the scattering by point impurities or isotopes (A is a proportionality factor) and the third term $(B_1+B_2)\omega^2T^4$ is the umklapp process for phonon-phonon with B1 and B2 as phonon parameters.

Wiedemann-Franz law gives a relationship between with the thermal conductivity and another material property, namely the electrical resistivity [12].

$$\lambda\rho = LT \tag{3.30}$$

where ρ is the electrical resistivity and L is the Lorentz number. This number is given in (3.31).

$$L = \frac{\pi^2}{3}\left(\frac{k_B}{e}\right)^2 T \tag{3.31}$$

with e as the electron charge and T is the absolute temperature.

3.4.2. Electrical Resistivity

When a metal is exposed to an electrical field, a drift of free electrons are created so we can define an electrical resistivity. This electrical resistivity is a measure of how strong a material are opposing the flow of an electrical current. Due to various scattering processes of the electrons, such as the thermal vibrations of the crystal lattice (phonons) and lattice imperfections, the conductivity will remain limited.
This is shown by Matthiessen's rule, an empirical statement, which gives the total electrical resistivityρ [18].

$$\rho = \rho_i(T) + \rho_r \tag{3.32}$$

where ρ_i is the temperature dependent phonon scattering resistivity and ρ_r is the imperfection scattering.

The insulating quality of a solid electrical insulator usually improves as the temperature is lowered due to accidental surface films of moisture become less conducting. All the regular cryogenic fluids are fine electrical insulators [19].

The electrical resistivity for aluminium, copper and stainless steel, which are commonly used at cryogenic temperatures, are shown in Figure 14, Figure 15 and Figure 16, all taken from [37].

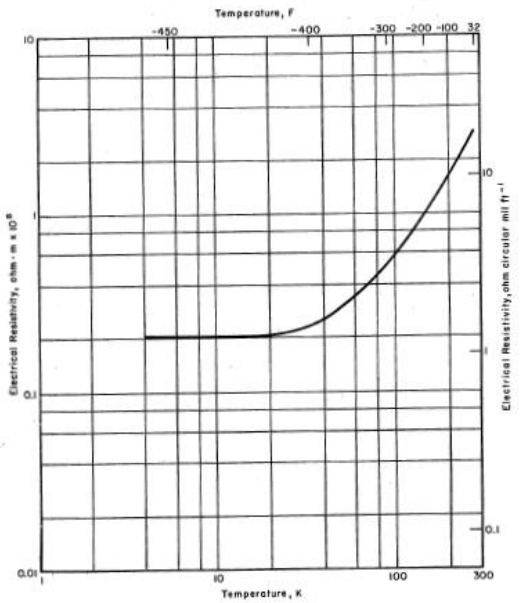

Figure 14. The electrical resistivity of aluminium alloy 1100-0.

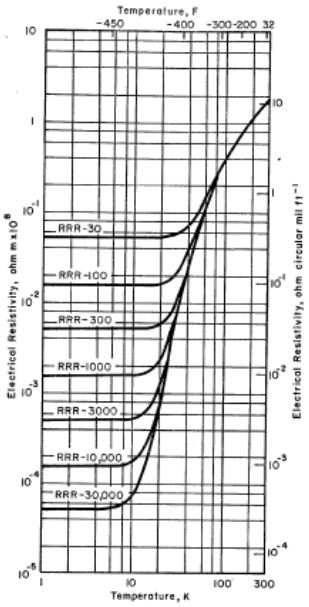

Figure 15. Electrical resistivity for copper vs temperature for various RRR-values. RRR (Residual Resistivity Ratio) a is purity indication, resistivity at 300 K / resistivity at 4.2 K.

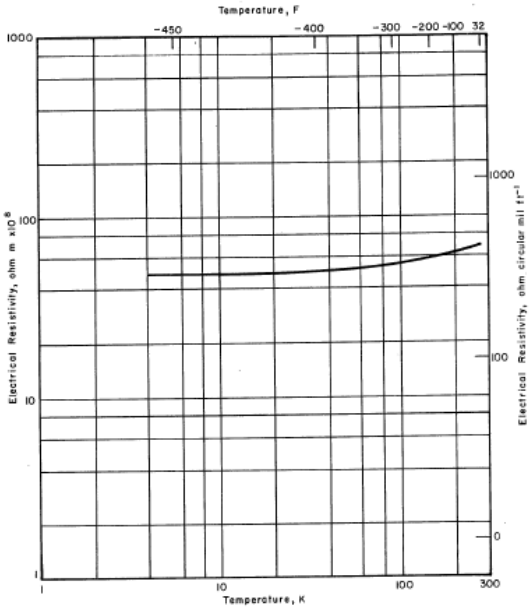

Figure 16. Electrical resistivity versus temperature for 304L stainless steel

Electrical resistivity has a reciprocal quantity, namely electrical conductivity, which measures a material's ability to conduct an electrical current. This gives equation (3.33).

$$\rho = \frac{1}{\sigma} \tag{3.33}$$

where ρ the electrical resistivity and σ is the electrical conductivity.

3.4.3. Specific Heat Capacity

Specific heat is defined as energy required to raise temperature of a unit mass of a substance by one degree [38]. As almost all physical properties of a solid, the specific heat also depends on the vibration or an atom's motion in a material.
Specific heat of any material at constant volume is defined as

$$C_V = \left(\frac{\partial U}{\partial T} \right)_V \tag{3.34}$$

where U is the internal energy, T is the absolute temperature, and V is the volume.
Similarly, specific heat at a constant pressure:

$$C_P = \left(\frac{\partial U}{\partial T} \right)_P \tag{3.35}$$

For metals the specific heat is due to both the conduction of electrons C_e and the contribution of the phonons (lattice vibrations) C_{ph} [12]:

$$C = C_e + C_{ph} \tag{3.36}$$

The free electrons contribution increase linearly with the *Sommerfeld* constant γ and the temperature.

$$C_e = \gamma T \tag{3.37}$$

The *Sommerfeld* constant is

$$\gamma = \left(\frac{\pi^2}{3} \right) D(E_F) k_B^2 \tag{3.38}$$

where $D(E_F)$ is an experimental estimation of the density of states at the Fermi level and k_B is Boltzmann's constant.
For the phonons the specific heat is described as equation (3.39) [18]

$$C_V = C_{ph} = 9R \left(\frac{T}{\theta_D} \right)^3 \int_0^{\frac{\theta_D}{T}} \frac{x^4}{(e^x - 1)(1 - e^{-x})} dx \tag{3.39}$$

where R is the universal gas constant per mole, T is the absolute temperature, θ_D is the Debye characteristic temperature.
The term x is a dimensionless variable

$$x = \frac{h\nu}{k_B T} \tag{3.40}$$

where h is Planck's constant and ν is the frequency of vibration.

The values of C_V (constant volume) and C_P (constant pressure) can be shown having a relation, namely through the Mayer relation [18]:

$$C_P - C_V = VT\frac{\beta^2}{\chi} \tag{3.41}$$

With β is the volume expansion coefficient and χ is the compressibility.

The specific heats for some materials are shown in Figure 17.

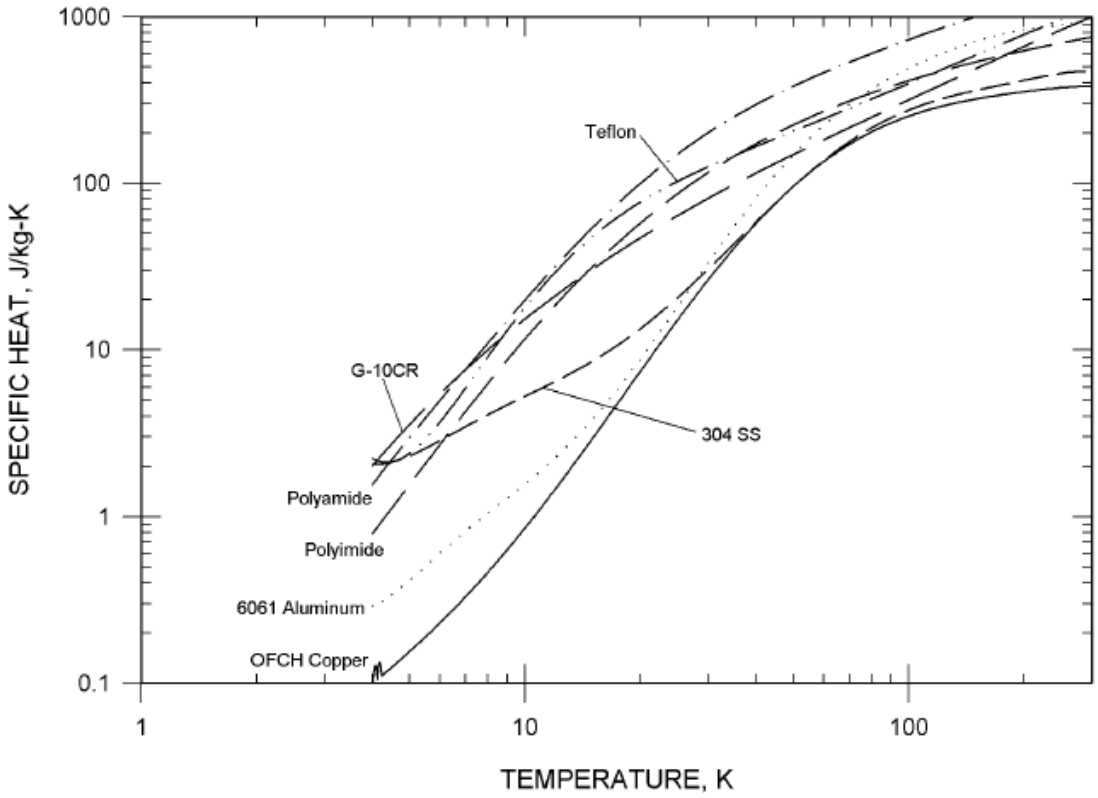

Figure 17. Specific heat of different materials [28].

At a constant volume the specific heat and the expansion coefficient α has an relation defined in the Grüneisen equation (3.42) [32].

$$3\alpha = \gamma\chi C_v \tag{3.42}$$

where γ is the Grüneisen constant.

3.4.4. Thermal Expansion/Contraction Coefficient

The coefficient of thermal expansion (CTE) does describe how the dimension of an object changes with a variation of the temperature. The fractional dimension change per temperature degree change at a constant pressure is the measure of CTE.

For the general case of a gas, liquid, or solid, the volumetric coefficient of thermal expansion is given by the equation (3.43) [24]

$$\alpha_V = \frac{1}{V}\left(\frac{\partial V}{\partial T}\right)_P \tag{3.43}$$

where V is the volume and $\partial V/\partial T$ is the volume change per unit change in temperature at constant pressure.

The linear coefficient of thermal expansion is related to the change of linear dimensions of a material with a temperature variation with a constant stress of the material. The pressure is ignored so the equation becomes

$$\alpha = \frac{1}{L}\frac{dL}{dT} \tag{3.44}$$

where L is the linear dimension and dL/dT is the rate of change of linear dimension per unit change in temperature.

The linear coefficients of thermal expansion for different materials are shown in Figure 18.

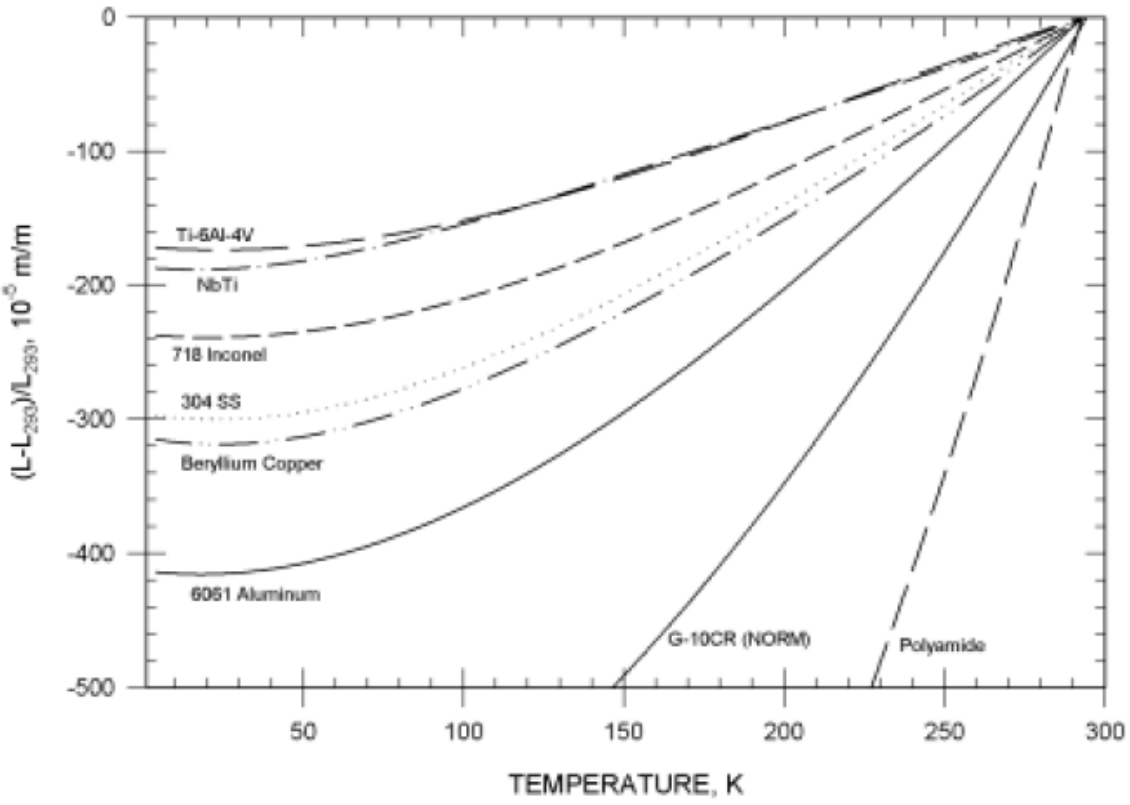

Figure 18. Linear thermal expansion of various materials [28].

Metals such as copper and copper alloys, together with aluminium and titanium have relatively mall coefficient of expansion while non-metals such as organic polymers have thermal expansion coefficients considerably higher than the metals [17].

For isotropic materials there is a relationship between the volumetric and linear coefficients of thermal expansion [24]

$$\alpha_V = \frac{\alpha}{3} \tag{3.45}$$

3.4.5. Mechanical Properties

3.4.5.1. Elastic Constant

The relation between stress and strain can be shown by the physical properties of elastic constants. Any elastically coupled force such as mechanical, thermal, magnetic, or electrical ones, can introduce either stress or strain.
This section will discuss some of the most commonly used elastic constants.

3.4.5.1.1. Compressibility

Compressibility K_T is a quantity of the relative volume change of matter as a response to a pressure (or stress) change.
The isothermal compressibility is defined as the following [24]

$$K_T = -\left(\frac{1}{V}\right)\left(\frac{\partial V}{\partial P}\right)_T \tag{3.46}$$

where P, T, and V is pressure, temperature, and volume.

3.4.5.1.2. Bulk Modulus

The inverse of the compressibility is called the bulk modulus B as defined in (3.47) and measures materials resistance to uniform compression [24].

$$B = \frac{1}{K_T} = -V\left(\frac{\partial P}{\partial V}\right)_T \tag{3.47}$$

With a high bulk modulus typically implies strong inter-atomic forces and a high cohesive energy. It does also show a high melting point and a high elastic-stiffness modulus.

3.4.5.1.3. Young's Modulus

Young's modulus, also known as the tensile modulus, describes the stiffness of an isotropic elastic material. This means that the Young's modulus calculate the variation in the dimension

of a bar (isotropic elastic material) under tensile or compressive loads. It can show how much a sample of a material can either extends under tension or shorten under compression.

Young's modulus E is defined by dividing the tensile stress σ by the tensile strain ε [39].

$$E = \frac{\sigma}{\varepsilon} \tag{3.48}$$

The equation (3.50) is another form of Hooke's law and Figure 19 show the Young's modulus for different materials.

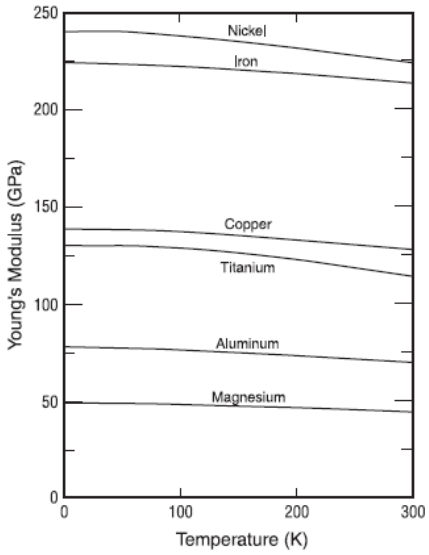

Figure 19. Temperature dependence of the Young's modulus for various materials [31].

3.4.5.1.4. Shear Modulus

The shear modulus is the elastic modulus used for the deformation, which occurs when a force is applied parallel to one face of the object while the opposite face is fixed by another equal force.

When an object with height L and cross section area A is experience a force F that is parallel to one face, the sheared face will be moved at a distance Δx. The definition of the shear stress is that the magnitude of the force per unit cross-sectional area of the face being sheared (F/A). Then the shear strain is $\Delta x/L$.

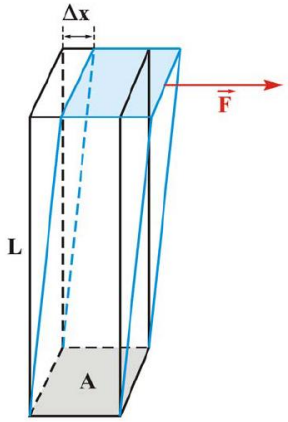

Figure 20. The definition of shear modulus [40].

Hooke's law for the shear conditions with the shear modulus G is defined as the ratio of the shear stress τ to the shear strain γ [12].

$$G = \frac{\tau}{\gamma} = \frac{F/A}{\Delta x/L} = \frac{FL}{A\Delta x} \tag{3.49}$$

3.4.5.1.5. Poisson's Ratio

When an object of a material is having a applied tensile or normal stress, it's being stretched in one direction and tends to get thinner in the other two directions. This involves a strain that is transverse to the direction of the applied stress (transverse) and a strain in the direction that is parallel to the applied stress (longitudinal) [12].
The *Poisson's radio* υ is shown as

$$\nu = -\frac{\varepsilon_{transverse}}{\varepsilon_{\text{longitudinal}}} \tag{3.50}$$

3.4.5.2. Emissivity

It was shown the emissivity plays a vital part in the radiation energy that is a heat input load to a component. As stated in *3.2.1 Heat Transfer - Radiation* the normal emissivity ε is the radiant energy emission that is normal to the surface and divided by the corresponding from a blackbody [24].

For electrical conductors the normal emissivity is proportional to its absolute temperature and also to the electrical conductivity as seen in equation (3.51) [41].

$$\varepsilon \approx \frac{1\cdot 10^{-4} T}{\sqrt{k_{e,273}}} \tag{3.51}$$

where $k_{e,273}$ is the electrical conductivity at 273 °K in Ω cm and T is the absolute temperature in °K. This is provided that the surfaces are smooth and oxide-free and the wavelength of radiation is not too small.

The emissivity of electrical insulators is related to the index of refraction n_r of the material, so the emissivity for electrical insulators is [24]:

$$\varepsilon = \frac{4n_r}{(n_r + 1)^2} \tag{3.52}$$

Since the index of refraction for most electrical insulators is less than 2, the emissivity of insulators is close to unity.

Some rules of thumbs can be suggested for emissivity of materials [24].

- Materials having the low emissivities also have the low electrical resistances.
- Emissivity decreases with decreasing temperature.
- The apparent emissivity of good reflectors is increased by surface contamination
- By alloying a metal increases its emissivity
- By treatment such as mechanical polishing of the surface layer of a metal, the emissivity is increased.

In practice, hemispherical emissivity ε_h is often considered, which takes into account radiant energy emission into a hemisphere (centred on the normal to the emitting surface). The following figures are the total hemispherical absorptivity (solid symbols) and emissivity (open symbols) for aluminium (Figure 21), copper (Figure 22), aluminium alloy and copper–zinc brass (63% Cu) (Figure 23) and stainless steel sheet 304 (Figure 24) [42].

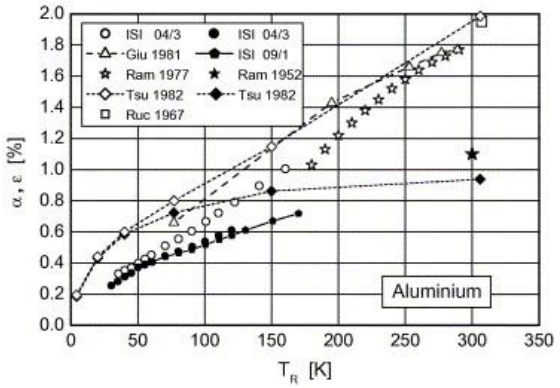

Figure 21. The total hemispherical absorptivity (solid symbols) and emissivity (open symbols) for aluminium.

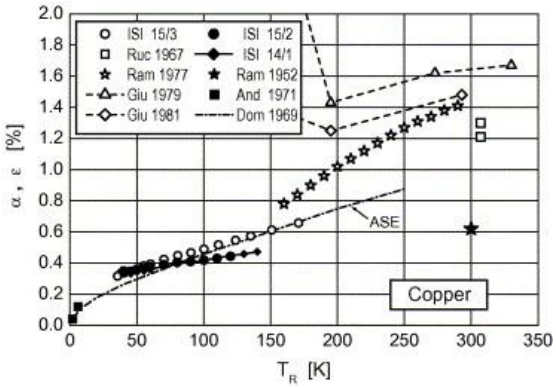

Figure 22. The total hemispherical absorptivity (solid symbols) and emissivity (open symbols) for copper.

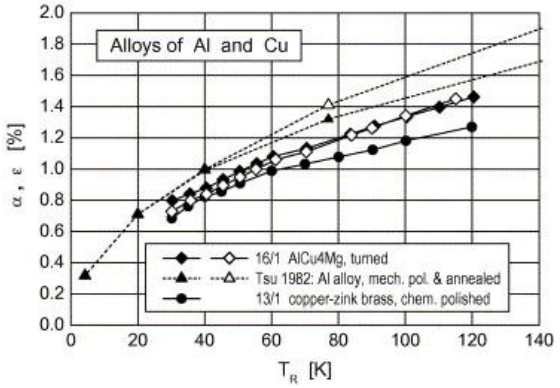

Figure 23. The total hemispherical absorptivity (solid symbols) and emissivity (open symbols) for aluminium alloy copper-zinc brass (63% Cu).

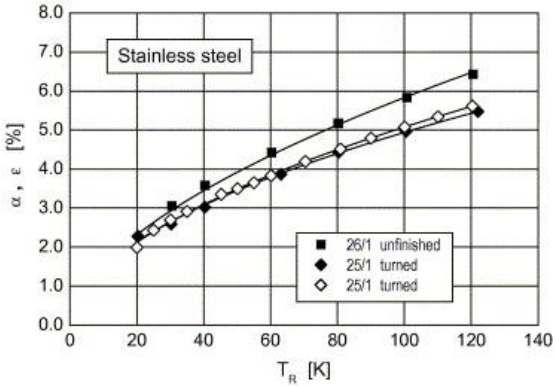

Figure 24. The total hemispherical absorptivity (solid symbols) and emissivity (open symbols) for stainless steel 304.

3.5. Eigen Frequency

The Eigen frequencies, also known as natural frequencies of vibration, are frequencies at which a system naturally vibrates once it has been set into motion.

The Eigen frequency ω is determining by (3.55) for an undamped free vibration of a single mass that only moves vertically, such as spring with a force created by the static deflection with a spring of stiffness *K* that supports a mass *M* [43].

$$\omega = \sqrt{\frac{Kg}{M}} \tag{3.53}$$

where g is the acceleration of gravity.

For a more complex system such in a cryostat, multiphysics simulations software, such as Ansys [44], can be used.

Chapter 4

Analysis of Band 5 Cold Cartridge Assembly

This chapter describes the thermo-mechanical modelling done by the author as part of the design and investigation of the Band 5 cartridge support and optical structure. The first section sets up a presentation of B5CCA and describes the details of the technical specifications. The second section shows design issues for the internal modelling with optimization of wiring and heat sink development as major issues. The chapter continues with investigation of thermal deformation and how it can affect the illumination efficiency. The thermal load of the optics structure due to radiation is presented followed by mechanical design with analysis of vibration, magnetic flux and stress.

4.1. Overview of the Band 5 Cold Cartridge Assembly design

For the presentation of the Band 5 Cold Cartridge Assembly (B5CCA), the author will follow the sources [45-47] and will go from the top to the bottom of the cartridge. As stated in the introduction, the ALMA Band 5 cartridge is a dual-polarization heterodyne receiver employing 2SB SIS mixers with IF band 4-8 GHz and covers the frequency 163-211 GHz. The basic cartridge structure is built upon a modular approach, where the base plate has an operating temperature of 300 K followed by 110 K, 15 K and 4 K stages. The plate at 300K is made of stainless steel, the 110 K stage of aluminium and both 15 K and 4 K stages of copper. These are separated by G10 fibreglass tubes for thermal insulation. The Band 5 cold cartridge is shown with its internal structure in Figure 25 and a picture of the first completed production B5CCA can be seen in Figure 26.

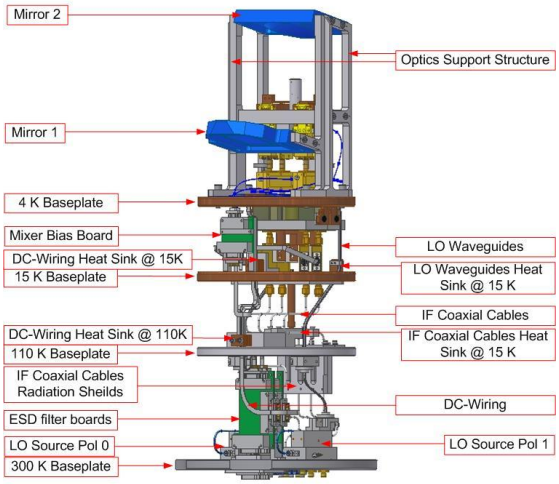

Figure 25. Band 5 receiver cold cartridge internal structure. The fibreglass spacers have been removed for better visibility.

Figure 26. Picture of the complete production B5CCA #1.

The ALMA Band 5 cartridge represents the lowest frequency channel of the ALMA frontend that employs *all-cold optics* and therefore has the largest mirrors among the other ALMA bands with cold optics. At the top of B5CCA, the optical support structure is manufactured of the aluminium alloys (EN7075 and EN5083, ALCA5). These light alloys were used due to the limitation of the 2 kg added mass at cold stages [48] and mechanical properties of these alloys suitable for precise machining. As seen in Figure 27, the optical structure consists of two mirrors, which are supported by two vertical brackets. It has a crossbar that provides a reference plane and acts as a support for the mixer assembly, which is integrated around the OMT (the orthomode transducer) that performs the polarisation separation. The additional vertical support bracket provides additional cooling and adds stiffness to the main support brackets. The optics structure has a design that is employing the guiding pins (dowel pins) of Ø1.5 and Ø4 mm and M5 screws attaching optical support brackets to the 4 K plate (see Figure 28). The idea of different pins sizes is explained in the section *4.3.2 Thermal Deformation of the Optics Structure*.

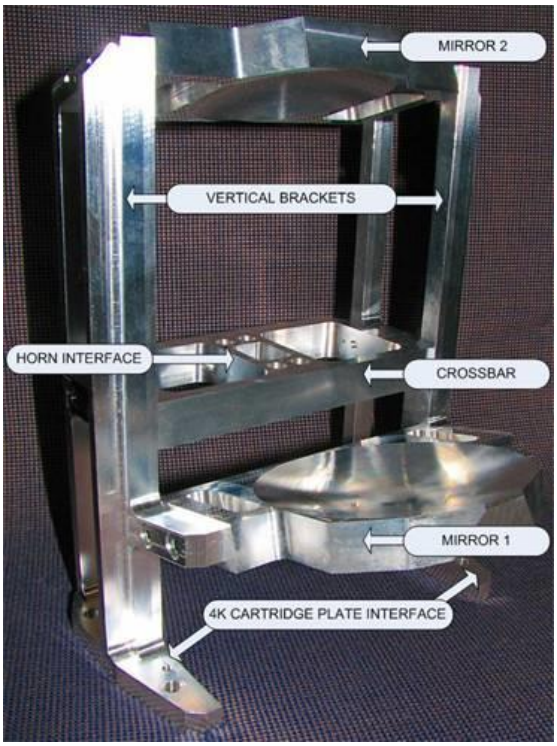

Figure 27. The B5CCA optics structure [47].

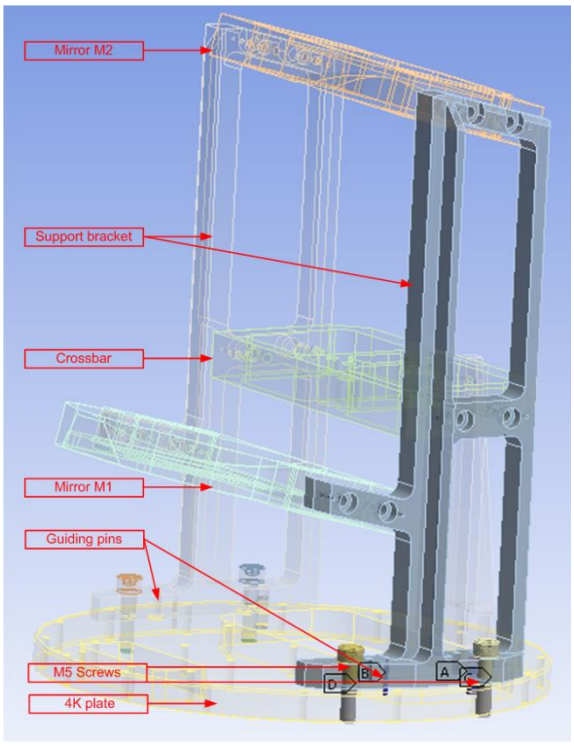

Figure 28. The optics structure with screws and pins attached to the 4K plate [49].

The parameters of the mirrors and the horn are based on design presented by M. Carter, *et al.* [50] and analyzed by M. Whale, *et al.* [51] with physical optics simulations to make sure that acceptable level of the cross-polarization and that is fulfils the specification.
The corrugated horn is in connection of the crossbar that is between the vertical optics support brackets and it acts as a mechanical interface to the mixer assembly. The corrugated horn is made of copper via electroforming and has 94 corrugations. The horn went through an optimization routine for providing the finest Gaussian fit of the main lobe while reducing the side-lobs below -30 dB level.

The OMT is based on the design of ALMA Band 4 cartridge suggested by Dr. S. Asayama and has a redesigned output of one polarization and slightly re-optimized dimensions using 3D EM electromagnetic simulation (CST Studio) [52]. To be able to use the same 2SB mixers for both polarizations, a 90-degree waveguide twist is added to the OMT output placed at the opposite sides. More details of the OMT can be found in [47].

The mixer blocks contain the SIS mixer substrate, which has mirrored layout for different DSB mixers constituting 2SB assembly and being placed facing the RF and LO signals in the waveguides whereas the IF outputs are directed towards the 300 K plate. For development details of the Band 5 mixer and the IF hybrid see reference [53]. On the top of the mixer blocks magnetic field coils are placed for suppression of the Josephson current and an extensive analysis for its optimization is presented in paragraph *4.5.2 Magnetic Flux Analysis.* The mixer assembly comprising the horn, the OMT and mixer blocks is shown in Figure 29.

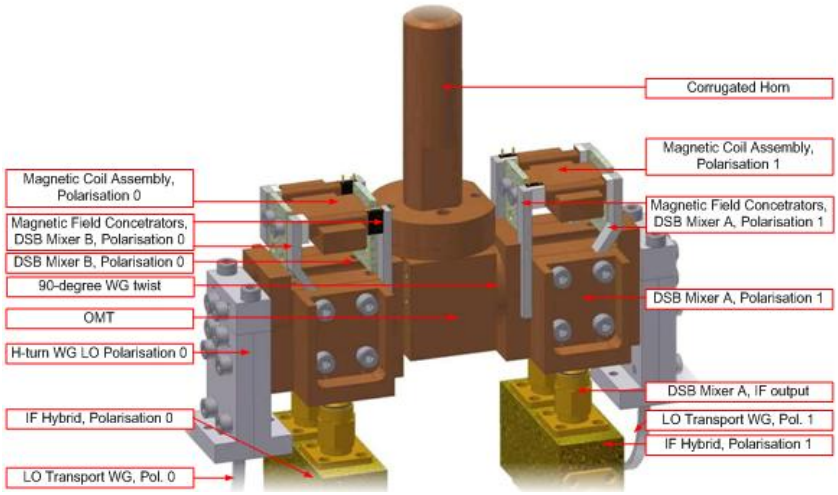

Figure 29. ALMA Band 5 Mixer Assembly [45].

The IF system that consist of the mixer block, IF hybrid, isolator and IF amplifier (Figure 30), is built along the vertical axis of the cartridge, because this was the only possible solution to fit the receiver part of the B5CCA along the optics. By using all the space between the 4 K and 15 K stages and doing a recess in the 15K plate resulted in a relatively long IF chain that may be exposed to potentially harmful mechanical stress as a result of difference in thermal contraction of the components made of different materials. By introducing a titanium intermediate piece in the IF support bracket, a similar solution was used by ALMA Band 9 for secure tightening of screws [54], the mechanical stress caused by difference in thermal contraction could be compensated. The titanium part is more discussed in the section *4.2.3 The Titanium Compensating Piece in the IF Support Bracket*. The cold IF amplifiers are 3 stage HEMT amplifiers with the first stage using InP HRL HEMT and the two other stages using GaAs HEMT transistor MGFC 4419G. Information of the IF amplifiers are available in [55]. The microwave cryogenic isolators between 4-8 GHz are coming from PAMTECH Inc with a minimum isolation of 18 dB and a maximum insertion loss of 0.5 dB [45].

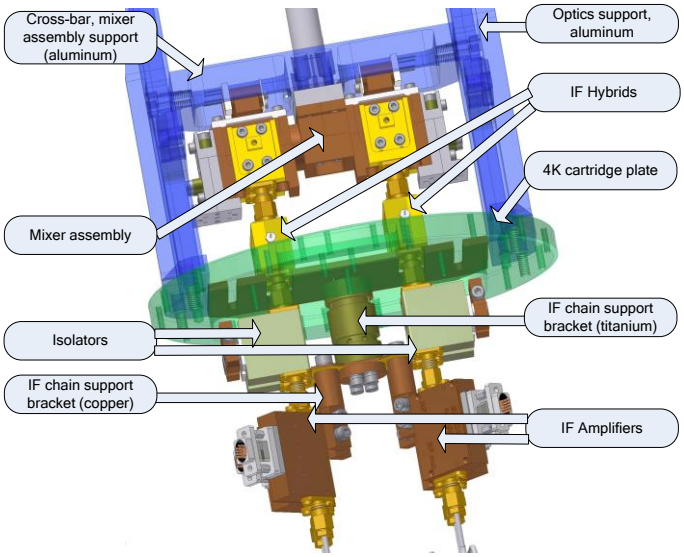

Figure 30. Picture of the Band 5 cartridge IF system that consist of mixer block, IF hybrid, isolator and IF amplifier. The IF support bracket is made of titanium (with copper inserted) to provide a good mechanical support and an effective cooling of the IF amplifiers [45].

The selection of the IF output coaxial cables were made with the consideration of finding a good balance between thermal load applied to the stages, and the cable RF losses. In particular, we revert from using the coaxial cables UT-85-SS-SS to UT-085B-SS (Micro-Coax [56]) cable as the latter provides a better balance of the thermal load and the RF losses. The frequency versus the insertion loss of UT-O85B-SS and UT-85-SS-SS for length of 0.305 m and 0.320 m are presented in Figure 31 [56].
The coaxial cable UT-085B-SS has a silver plated beryllium copper central conductor with a PTFE dielectric and 304 stainless steel outer conductor shell.

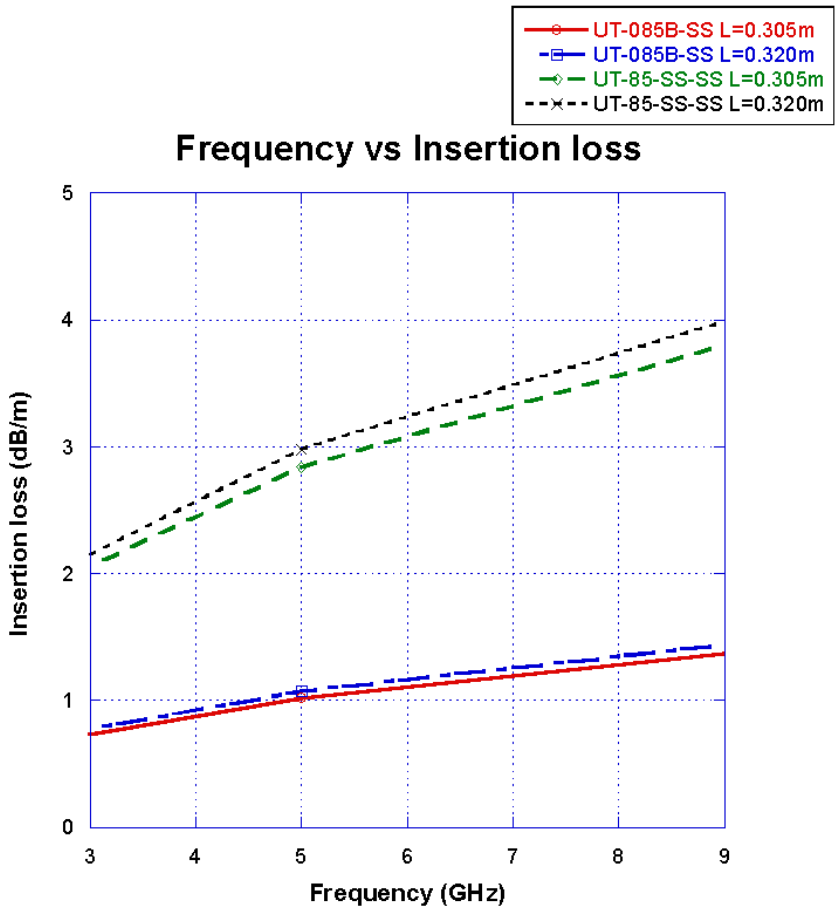

Figure 31. The frequency verses the insertion loss of UT-O85B-SS and UT-85SS-SS for length of 0.305m and 0.320m.

The path of the IF cables to the 300 K plate goes through heat sinks that are attached at the 15 K stage and has a thermal shield installed at 110 K for reducing radiation from the 110 K plate. The IF cables are also shaped to relief stress caused by thermal contraction and are produced by SSI Cable Corp. [57] with welded SMA contacts with anti-torque nut as shown in Figure 32.

Figure 32. IF cable assembly with 110K thermal shield installed; the two stress-relief half-loops are made for the cable length between the base plate and the 110 K plate and the 110 K and 15 K plates.

For the LO transport, an oversized stainless steel waveguide WR-10 (2.54 mm x 1.27 mm) with a wall thickness of 0.3 mm was used. Non-gold-plated WR10 stainless steel waveguide was chosen to provide the required thermal isolation. The WR10 waveguides have slightly oversized dimension for the LO frequencies (native WR5 band) giving about 7 dB RF loss and providing expected level of the high order mode excitation better than -10dB [58]. Figure 33 shows the longer WR10 waveguide with mounted 110 K heat sink on one side and an integrated transition WR10/WR5 with 90-degree H-plane turn on other side. The heat sink in the middle of the waveguide is at 15 K plate of the cartridge

Figure 33. The longer WR10 waveguide connects the 110K and the mixer assembly for respective polarization. The waveguide is produced by Aerowave Inc [59].

The LO sources for Band 5 are developed by Rutherford Appleton Laboratory, with a final multiplication stages comprising of an active tripler followed by a isolater and with final stage times two multiplier (Figure 34). The source is integrated inside the B5CCA at the 300K plate (vacuum side) with coaxial K-type feed-through input

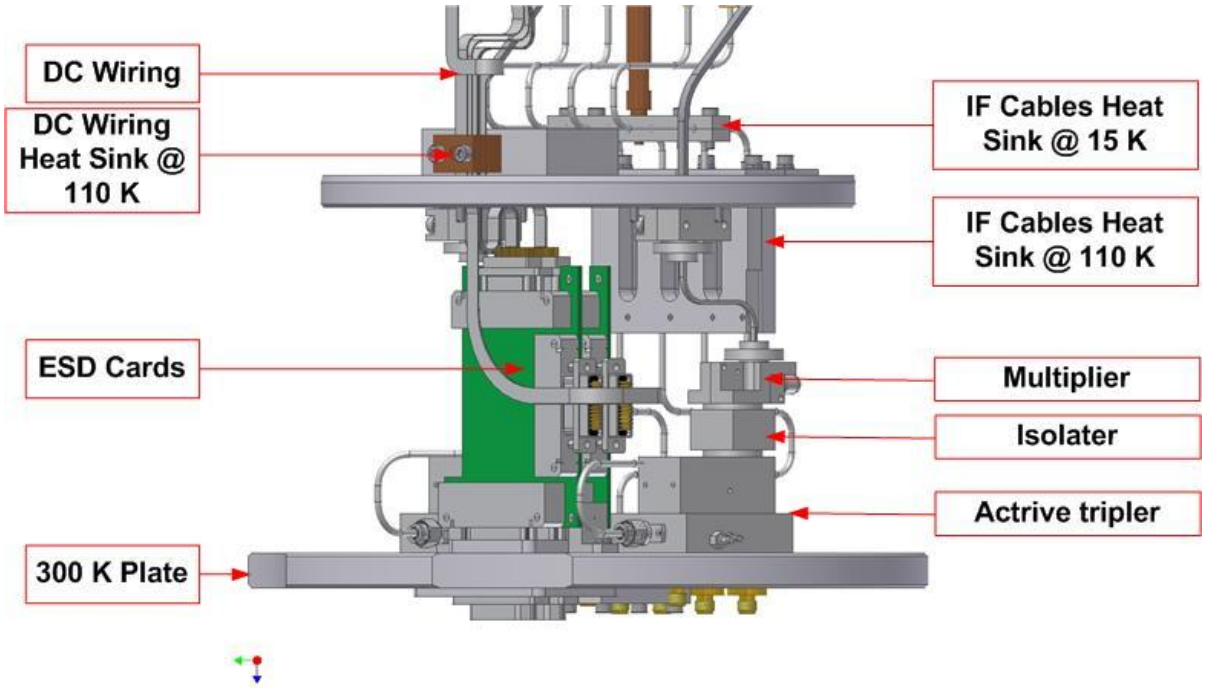

Figure 34. B5CCA components at the 300K plate.

The Band 5 receiver cartridge uses Glenair DC interface connector with ESD cards directly attached to it at the vacuum side at 300 K plate (see Figure 34). The purpose of the ESD cards is to provide required ESD and over-voltage protection of the HEMT amplifiers, SIS mixers and other components. Another purpose of the ESD cards was also providing division of the wiring. Another printed circuit board is placed at 15K plate and provides the SIS DC bias with resistor circuitry converting 6-wire bias into two-wire bias for every 4 SIS mixers.

The Band 5 cartridge internal DC harness should supply all voltages and currents to the SIS mixers, HEMT amplifiers, temperature sensors, magnetic coils and deflux heaters. The twisted pair option was chosen to prevent interference and crosstalk. The DC harness employs 48 twisted pairs with the current ranging from 10 μA up to 10 mA. The design considered the choice of optimal conductor for wires, optimisation of the length and the location of the thermal sinks. The optimization of the heat flow and dissipation was based on the computation of the inter-stage heat flux balance as discussed in paragraph *4.2.1 DC Wiring Length*. As a result, 2 and 12 twisted pairs looms based on 0.102 mm constantan wire (SWG-42) were chosen providing a compact design of the DC harness. The loom was equipped with thermal sinks at 110 K, 15 K and 4 K stages. For the 4 K stage wiring, the phosphor bronze twisted pair was chosen with the wire diameter of 0.127 mm (AWG-36), due to less electrical resistivity (54 Ω/m [30] for constantan compared to 9 Ω/m [29] for phosphor bronze at 4K).

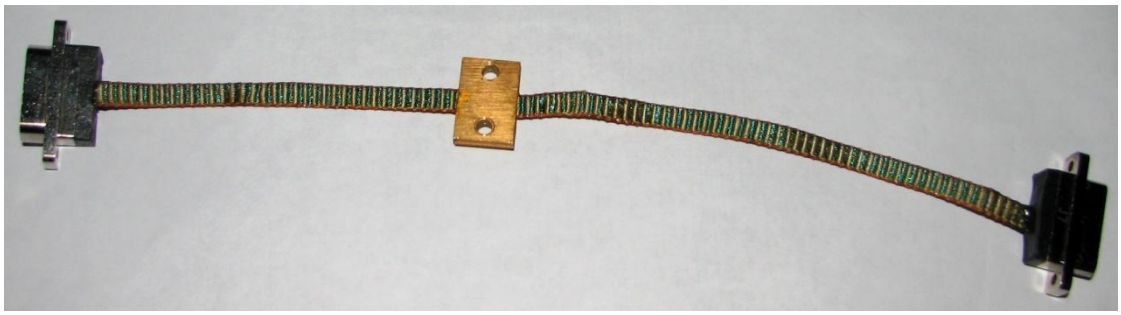

Figure 35. A DC cable assembly with 110K heat sink installed; the bus of 12 twisted pairs with Constantan wires 0.1 mm diameter. The cable in the picture is produced by SSI Inc. and use Glenair connectors with the soldering part embedded into protective Stycast cover.

The DC cables looms are divided into several ones. One loom is dedicated for the SIS mixer DC bias only and other loom are separate for the DC biasing of IF amplifiers for each polarization. A fourth wire bus carries magnetic coil currents, defluxer and temperature sensor connections. These separations was done to reducing EMI for SIS DC bias and HEMTs

4.1.1. Specifications

The Band 5 cartridge design follows the specifications [4, 17, 18] set by ALMA. This paragraph will discuss those that have an effect on the cryogenic and mechanical work of the cartridge components.

TABLE 3 shows the specified temperature ranges [48] and the chosen values for the analysis. The fixed values of the temperature were chosen in an assumption that it should not noticeably affect results of thermo-mechanical modelling while substantially simplifying the analysis procedure.

TABLE 3. ALMA FE STAGES TEMPERTURE

	Base plate	**Stage 1**	**Stage 2**	**Stage 3**
Specified range (K)	(TBD)	70-130	10-18	4 (max)
Chosen values (K)	300	110	15	4

4.1.1.1. Heat Load Specifications

There are three main receiver functional states, referred to the power dissipation level – operating, standby and non-operating modes [60], [61]. TABLE 4 summarizes specification for passive heating load, which is associated with the non-operating mode and the total heat load related to the operating mode. The passive heating load includes an inter-stage radiation heat exchange and heat power through the cartridge receiver components – waveguides, coaxial cables, and DC wiring. The total dissipated load includes, besides passive heating, electrical power dissipation related to the DC (high-resistive) cryo-wiring, the IF amplifiers, magnetic coils (B5CCA employs non-superconducting coils) and SIS mixer DC-bias circuit dissipation.

TABLE 4. HEAT LOAD SPECIFICATIONS

	Base plate	**Stage 1 (110K)**	**Stage 2 (15K)**	**Stage 3 (4K)**
Passive heating (mW)	(TBD)	700	95	5
Passive + active heating (mW)	(TBD)	850	162	41

4.1.1.2. Weight Specification and Eigen Frequency

The specification for the mass states that all added components to the cold stages (4K, 15K and 110K) shall not exceed a mass of 2 kg and lowest Eigen frequency is limited to 70 Hz [61].

4.1.1.3. Optical Specification and Tolerance Budget

For all ALMA bands, the aperture efficiency factor (η_{ap_FE}) of the front end optics shall exceed 80% [62] and depend among other factors (like edge-taper efficiency, signal loss due to the secondary reflector (non-uniform amplitude distribution and phase), spillover efficiency) on *tolerances* in positioning of the B5CCA optics components.

The tolerance budget of the optics for B5CCA is shown in TABLE 5. The budget is based on Dr. B. Lazareff's suggestions [63] for the alignment tolerances for ALMA optics.

TABLE 5. OPTICS TOLERANCE BUDGET. FOTNOTE 1 INDICATE THE INPUT ANGULAR INTO OUTPUT ANGULAR CONTRIBUTION WHILE FOTNOTE 2 IS THE INPUT LINEAR INTO OUTPUT ANGULAR CONTRIBUTION.

Element	**Horn**	**First cold Mirror**	**Second cold Mirror**
Interface number	2	1	1
Coeff. (rd/rd)[1]	8.2E-3	2.17	2
Angular tolerance single element (rad)[1]	1.5E-3	4.0E-4	4.0E-4
Contribution (rad)[1]	1.2E-5	8.3E-4	8.0E-4
Coeff. (rd/mm)[2]	1.7E-2	3.1E-2	1.5E-2
Linear tolerance position single element (mm)[2]	2.0E-2	1.0E-2	1.0E-2
Contribution (rad)[2]	3.4E-4	3.1E-4	1.5E-4
Worst case (rad)	2.44E-3	System goal (rad)	3.3E-3

4.2. Optimization of Band 5 cartridge Design

The optimization of the cartridge design was a group effort done by the author and other members at GARD. This paragraph presents the work done for optimization of design for a number of cartridge components, such as heat sinks, DC wiring, thermal shielding of the IF-cables and the IF support bracket.

4.2.1. DC Wiring Length

As described in the section *4.1.1.1 Heat Load Specifications*, there are three sources of the thermal load to be considered for the cartridge: radiation, thermal conductivity and electrical power dissipation. Specifications define the upper limit of the thermal load as an additional value to the thermal load of the existing blank cartridge. Through this thesis, the author will use the term "thermal load" in the sense of the added value. At 4 K stage, the specified thermal load is as little as 41 mW in the operating and 5 mW in the non-operating modes (see TABLE 4). The estimated electrical power dissipation of the IF amplifiers and the magnetic coils is about 34 mW. Thus, the total thermal load at 4K stage as a result of the thermal conductivity in the DC wiring, the LO waveguides and the IF coaxial cables according to the above calculations should not exceed 5 mW in the non-operating and 7 mW in the operating mode.

In the non-operating mode, the DC wiring thermal load is associated with the thermal conductivity and radiation. The heat influx through the DC wiring due to conductivity was investigated for a single constantan- or phosphor bronze wire with the corresponding temperature boundary condition on the places of the thermal sink locations.

Operating mode requires more complex approach for the correct estimation of the thermal load and accounts, besides the thermal conductivity, the electrical power dissipation within high-resistive DC wiring. The RF power dissipated in the IF coaxial cables and LO waveguides was not taken into account as negligible.

In order to optimize the balance between the conducting heat flux and the heat developed by DC current in the wires, some guidelines is to be used. The heat flow due to the thermal conductivity is proportional to the cross section and inversely proportional to the length of the wire as clearly follows from the equation (3.8) in the section *Heat Conduction*. This favours usage of a thin wire with long length and a low thermal conductivity. However, since there is a DC power dissipation due to the wire resistance, the thicker and short wires will be advantageous. This leads to an equation for a steady energy balance [32]:

$$\frac{d}{dx}\left(\lambda A\frac{dT}{dx}\right)+\rho\frac{I^2}{A}=0 \tag{4.1}$$

where $\rho(T)$ is resistivity and I is the current through the wires with the boundary conditions $T(0)=T_L$, $T(L)=T_H$.
With condition $x=0$, the heat Q_L is:

$$Q_L=\sqrt{Q_H^2+I^2\int_{T_L}^{T_H}2\rho(T)\lambda(T)dT} \tag{4.2}$$

Where Q_H is the heat at $x=L$. When $Q_H=0$ equation (4.2) is minimized:

$$Q_L^{\min}=I\sqrt{\int_{T_L}^{T_H}2\rho(T)\lambda(T)dT} \tag{4.3}$$

By using the Fourier conducting law (4.4) [64].

$$\frac{dx}{A} = \frac{\lambda}{\dot{Q}} dT \tag{4.4}$$

and integrate with boundary conditions T_H and T_L, the optimal wire dimension is given in (4.5).

$$\frac{L}{A} = \int_{T_L}^{T_H} \frac{\lambda(T)dT}{\sqrt{Q_H^2 + I^2 \int_T^{T_H} 2\rho(\tau)\lambda(\tau)dT}} \tag{4.5}$$

At $Q_H=0$ equation (4.5) becomes:

$$\frac{L}{A}(Q_H = 0) = \frac{1}{I} \int_{T_L}^{T_H} \frac{\lambda(T)dT}{\sqrt{\int_T^{T_H} 2\rho(\tau)\lambda(\tau)dT}} \tag{4.6}$$

This shows that the optimal wire dimension depends of the materials properties (thermal conductivity, resistivity) and the current, temperatures and the heat Q_H.

Both, the dependence of the thermal conductivity and the resistance were taken into account during the simulation with ANSYS Multiphysics Software [44]. The DC wiring simulation was provided for 12 twisted pair loom for the layout, shown in Figure 36 for different loom lengths and the currents. The length parameter represents the wiring length between 15 K and 4 K thermal sinks. The simulation results are presented at the contour plot of the thermal load, Figure 37. It covers a range of lengths and currents for fixed values of the dissipated power, related to the 4 K. The contour plot represents a simple physical meaning, i.e., at small length of the loom, the thermal conductance dominates in the thermal load and with the length increased, the thermal conductance influence of the wire is decreasing while the dissipation due to the resistance is increasing.

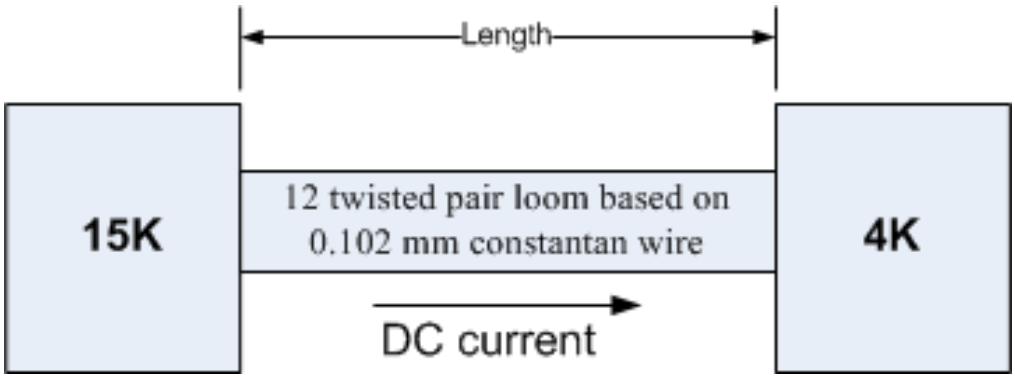

Figure 36. The layout for the DC wiring simulation.

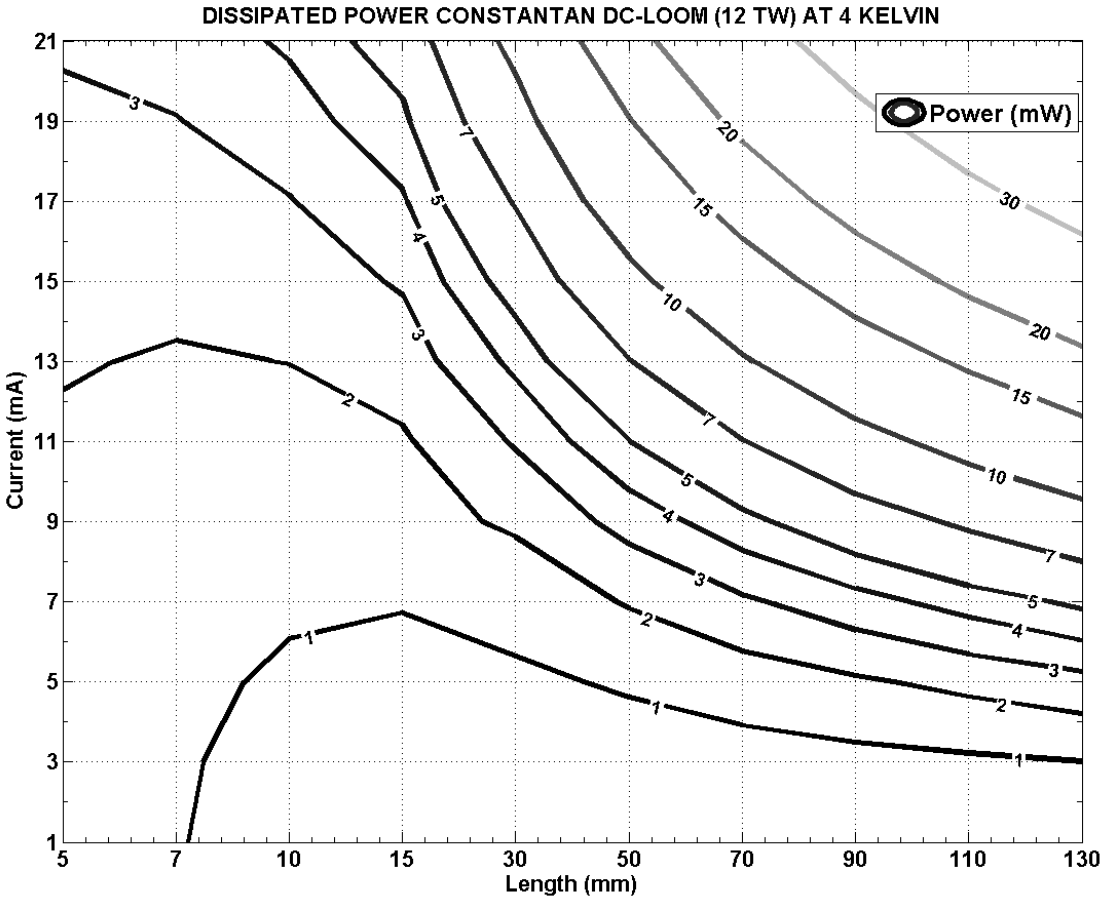

Figure 37. Contour plot of the dissipated power from a 12 twisted pair loom with constantan wire SWG-42 at 4 Kelvin plate.

According to Figure 37, the optimal length for the maximum current through the loom, which can be driven with an allowed heat influx, is such when the dissipation and the thermal conductance equalize at 1 mW in the loom is around 15 mm. This length was not implemented since the actual distance between 15 K and 4 K stages is somewhat longer. A possible way to implement optimum wiring configuration would be using 15 mm cryogenic wire soldered with copper wire with high conductivity. However, unless the cartridge design fulfils the specification thermal load requirements, such complication of the harness fabrication (also, potentially less reliable because of the increased number of contact points) cannot be justified. For B5CCA, the actual length was determined from the physical realization requirement within the range from 110 to 130 mm.

The total thermal load due to the thermal conductivity for all ALMA Band 5 cartridge internal wiring/cabling/waveguides is presented in TABLE 6, while the dissipated electrical power by the DC wires was analysed for amplifiers' wires (5 and 3 mA), mixer DC bias current wires, temperature sensors (10 μA), and the magnetic coil current wires (2 mA) (TABLE 7).

TABLE 6 POWER DUE THERMAL CONDUCTIVITY FOR ALMA BAND 5

Internal Wiring	**110 K Stage Power (mW)**	**15 K Stag e Power (mW)**	**4 K Stage Power (mW)**
DC wires	19.4	9.24	0.07
IF coaxial cables	196	110	3.16
LO waveguides	214	24	0.58

TABLE 7. DISSIPATED ELECTRICAL POWER APPLIED TO STAGES

Component	**110 K Plate (mW)**	**15 K Plate (mW)**	**4 K plate (mW)**
Amplifer DC wires (5 mA)	2.61	1	0.36
Amplifer DC wires (3 mA)	1.53	0.58	0.14
Mixer DC bias wires	0.01	0.13	0.01
Temperature sensors (10 μA)	0.01	0.03	0.01
Magnetic coil wires (2 mA)	1.46	0.55	0.12

4.2.2. Development of heat sinks

The development of the heat sink has gone through various iterations during the prototyping process of the B5CCA.

For reducing the thermal influx through cables, the IF-cables, LO waveguides and DC wiring has different heat sinks and has gone through its own development of the heat sinks.
The first generation of the heat sinks for the internal cabling is shown in Figure 38, Figure 39 and Figure 40. In these versions the heat sink at both 110 K and 15 K for the IF-cables are connecting through all IF-cables. The heat sinks big mass of copper has a good ‘cooling’ efficiency due to the thermal conductivity.
The heat sinks size for the LO waveguides is smaller. Since the waveguides are only of stainless steel, the mass of the copper could be reducing in the mind of the mass specification and achieving a good cooling.
The first generation of the DC wiring had parts pressed together as the heat sinks with connection to the different temperature stages. Further development of the DC wiring heat sinks are shown in Figure 41. This generation was redone for fixing the position of the DC wiring heat sinks due to concern of the heat load through the wiring. Also to have a better rigidity of the cartridge internal parts was another concern.

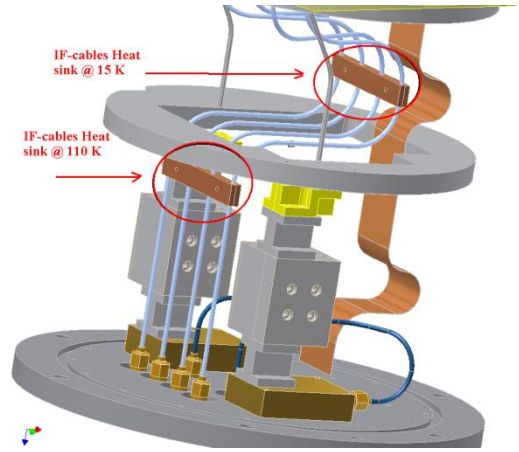

Figure 38. The first version of heat sinks for IF-cables.

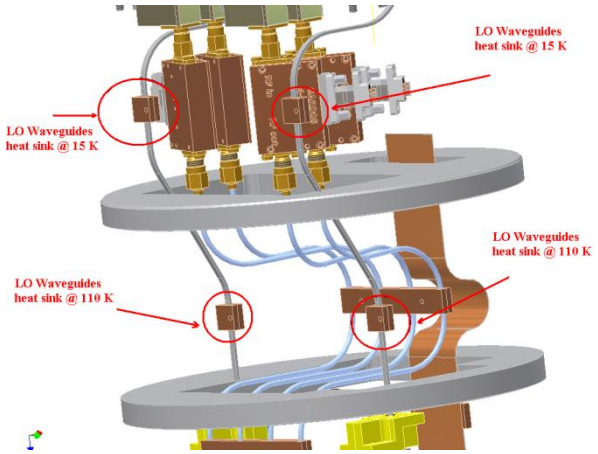

Figure 39. The first version of heat sinks for LO-waveguides.

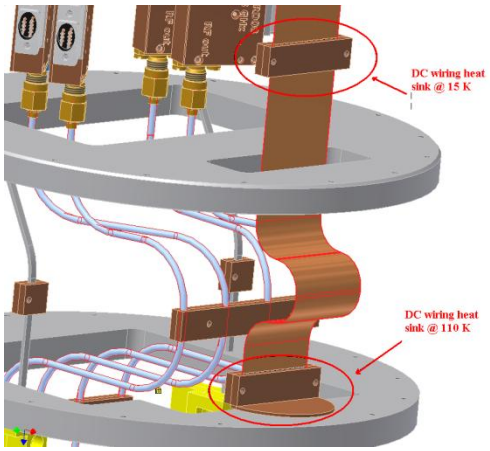

Figure 40. The first version of heat sinks for DC wiring.

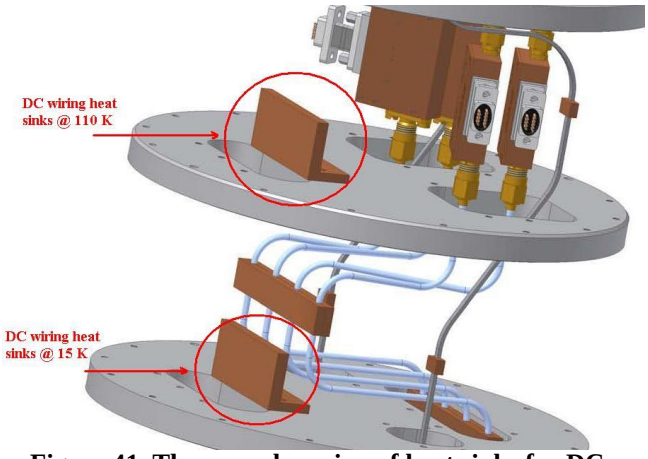

Figure 41. The second version of heat sinks for DC wiring.

Figure 42. The third version of heat sinks for DC wiring.

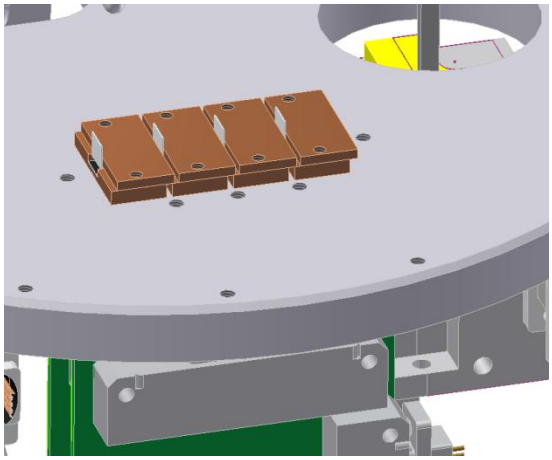

Figure 43. Placement of the third generation of DC wiring heat sinks at the 110 K stage.

The concern of having the different DC looms glued together at the common heat sinks due to thermal stress between the looms and the heat sinks when cooling down made it necessary to continue the development of the heat sinks. This lead to a decision to separate the heat sinks of the looms from common ones to individual ones.

The third generation DC wiring heat sink is shown in Figure 42 and consists of two copper blocks where one edge of the bottom and top part had a chamfer of 45˚ to decrease stress in the looms. The black part is cryogenic compatible, heat conducting epoxy and the cable loom is in white colour. The placement of these heat sinks at the temperature stages are shown in Figure 43, Figure 44, Figure 45 and Figure 46.

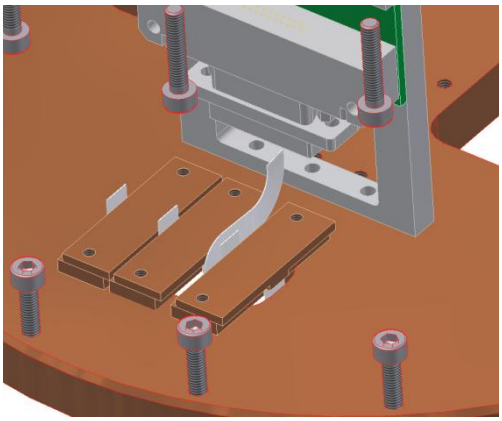

Figure 44. Placement of the third generation of DC wiring heat sinks at the 15 K stage.

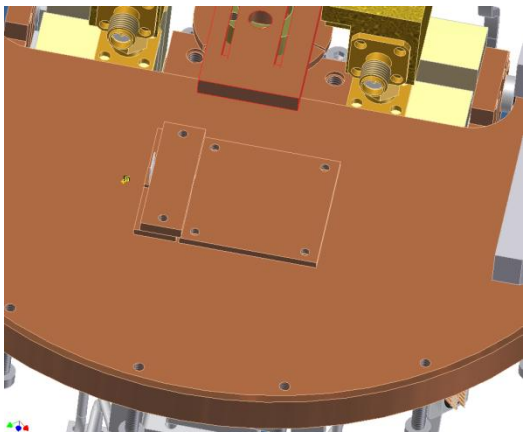

Figure 45. Placement of the third generation of the DC wiring heat sinks at the 4 K stage.

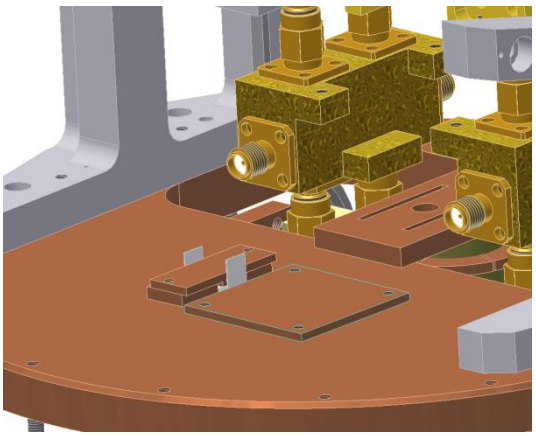

Figure 46. View from another direction of the DC wiring heat sinks at the 4 K stage.

After several iterations the finalized generation of the heat sinks for the internal cabling has the following solutions.
For the DC wiring some change was done of the heat sink. The gold plated copper blocks consist of one thinner flat half and another thicker half with a recess for the loom; both halves have chamfered edges to avoid damaging the loom (Figure 47 and Figure 48).

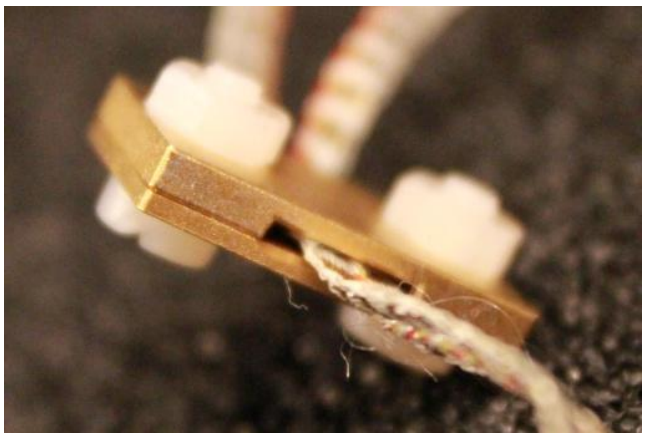

Figure 47. DC wiring heat sink done by Cryoconnect Tekdata [65].

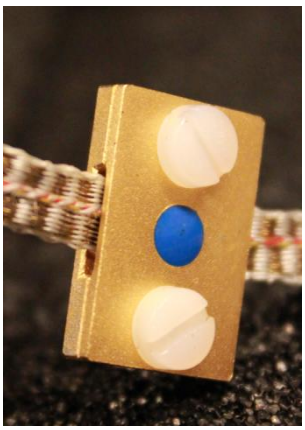

Figure 48. The heat sink from another direction.

Another difference compared to the previous version is that the heat sinks are mounted perpendicular to the cartridge plates, which ensures heat sink planes are always along the loom. Because of that, no bending of the loom at the heat sink edge and, correspondingly, no damage occurs.

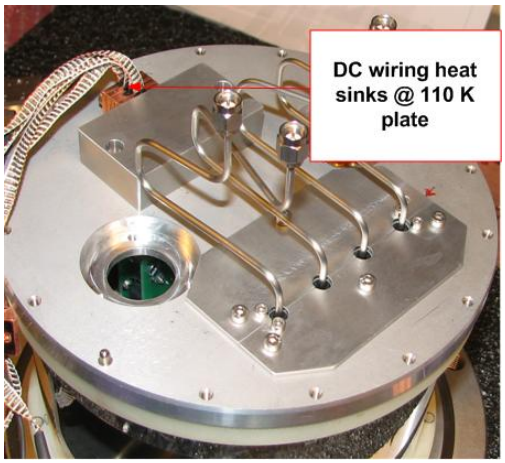

Figure 49. The DC wiring heat sinks at the 110 K plate.

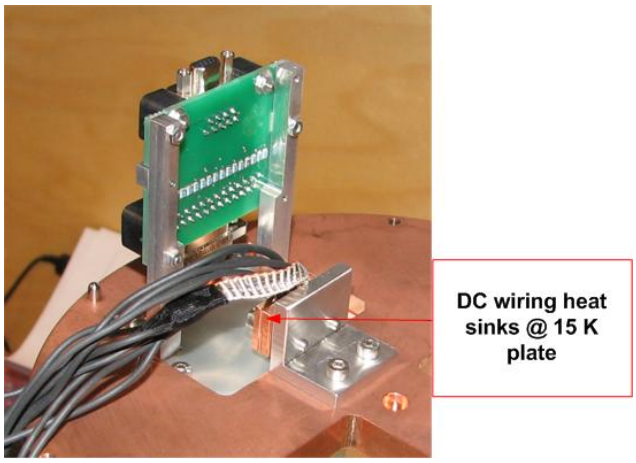

Figure 50. The DC wiring heat sinks at the 15 K plate with support.

Figure 51. The DC wiring heat sinks at the 4 K plate. The aluminium cover plate is to prevent thermal radiation coming through and add to the heat flux at the 4 K plate.

Heat sinks for the IF-cables are in the final version different at the different temperature stages. At the 110 K stage, a thermal shield was introduced due to thermal radiation coming from the 110 K plate. The thermal shield is done of aluminium alloy due to mass consideration (Figure 52).

For the 15 K heat sink, it is located just above the 110 K stage but with a copper thermal link coming from the 15 K stage. This solution was implemented due to the strict heat loads specifications for B5CCA. For fulfilling the specifications of the Eigen frequency of the cartridge the thermal link was a solid cylinder of copper. For reducing the weight and easy machining, the heat sinks material is aluminium (Figure 53).

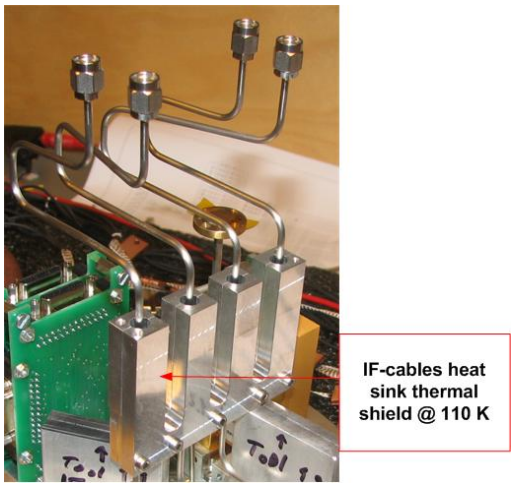

Figure 52. The IF-cables heat sink thermal shield at 110 K.

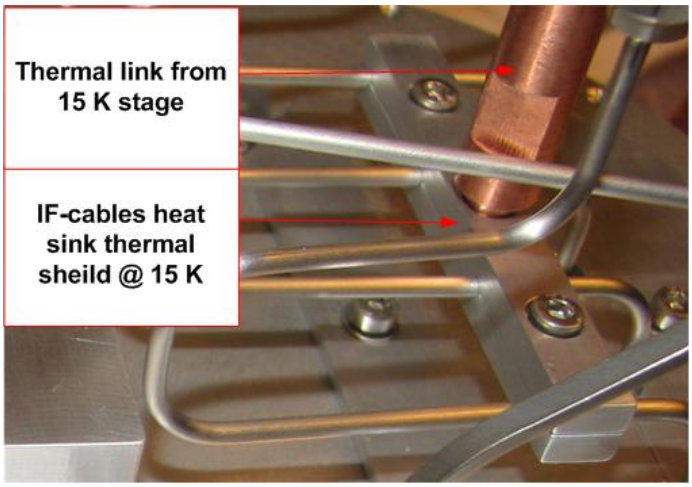

Figure 53. The IF-cables heat sink thermal shield at 15 K with the thermal link from the 15 K stage.

The LO waveguide consists of two parts. The 110 K heat sink is introduced between the first piece of the LO waveguides (Figure 54) with the transition WR5/WR10 and the second piece of the LO waveguide (Figure 55).

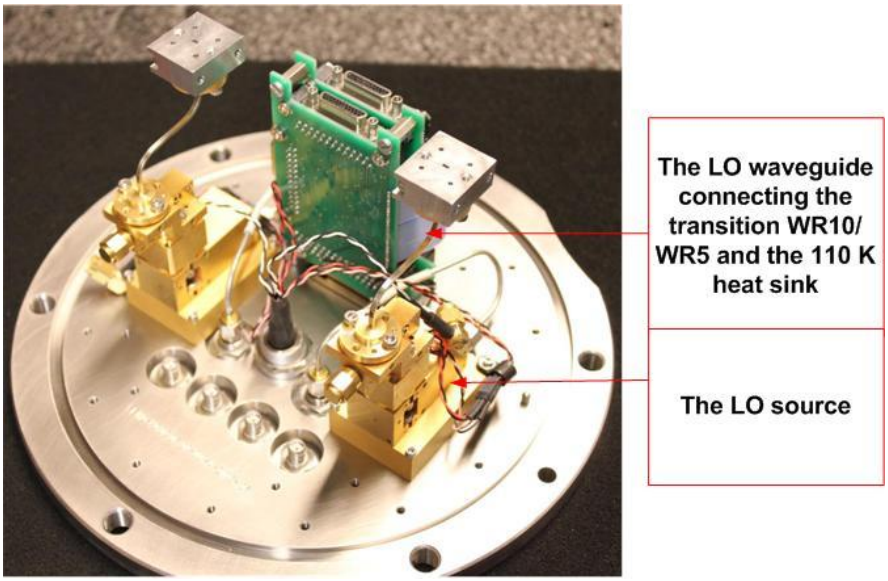

Figure 54. The LO waveguide connecting the transition WR10/WR5 and the 110 K heat sink from the LO source.

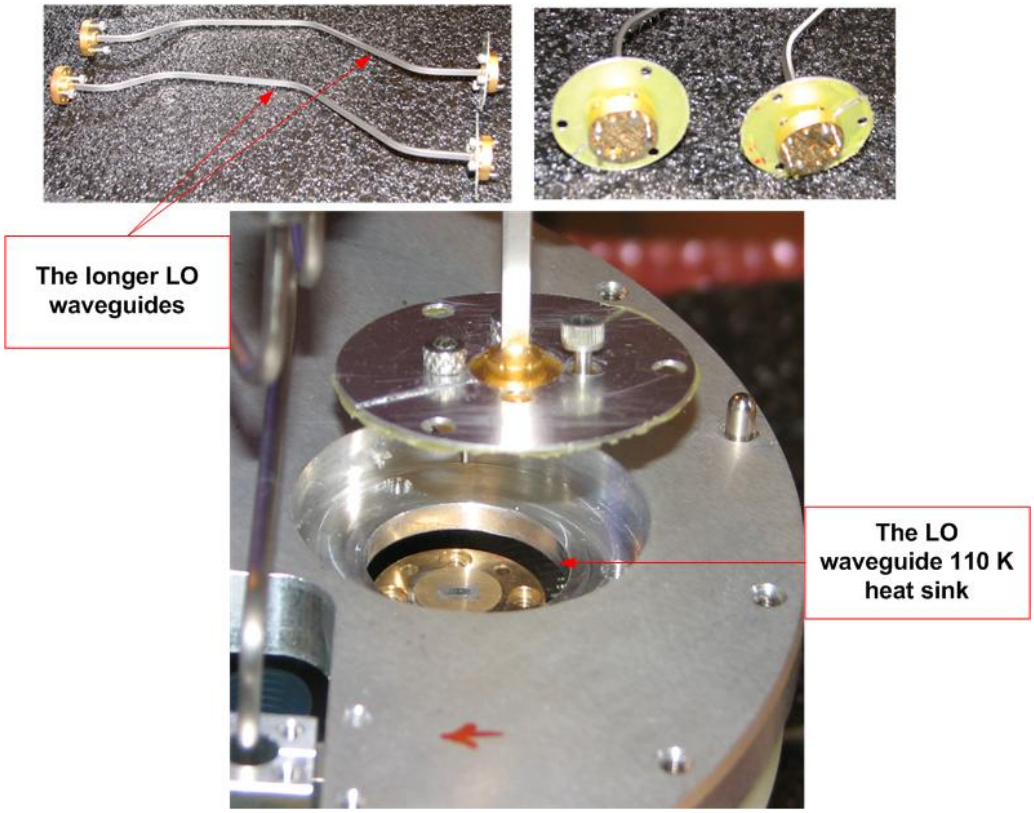

Figure 55. The longer LO waveguide with the 110 K heat sinks.

At 15 K stage the heat sinks is a combination of the materials aluminium and thin copper layer which connects the LO waveguide with the 15 K stage (Figure 56).

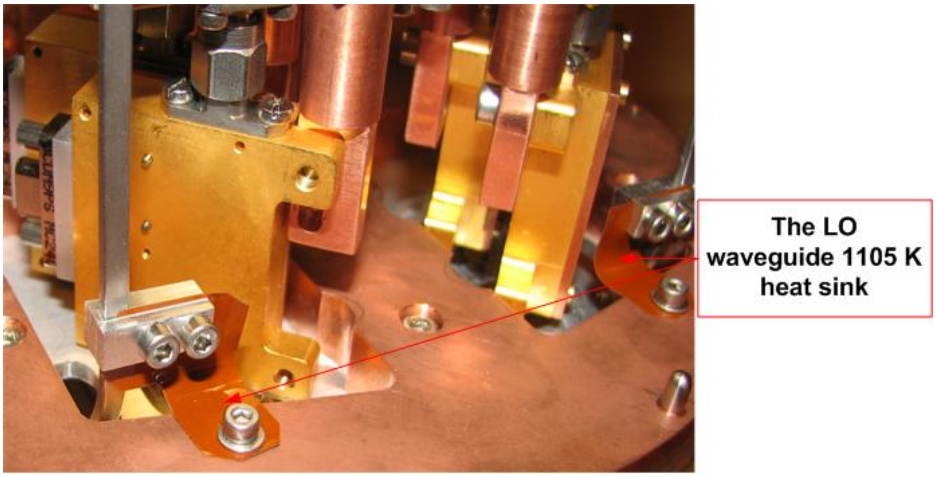

Figure 56. The LO waveguide heat sink at the 15 K stage.

4.2.3. The Titanium Compensating Piece in the IF Support Bracket

The long IF chain (see Figure 30) introduces the risk that due to thermal contraction during cooling from room temperature to 4 Kelvin the chain and its support are made of different materials (stainless steel, aluminium, copper etc.), may develop dangerous mechanical stress, which may cause damaging of certain components of the IF chain. The model used for optimization of the IF chain support bracket was simplified in assumption of linear deformation along the IF chain.
The analysis result is shown (Figure 57) that deformation of the IF-chain of 0.604 mm

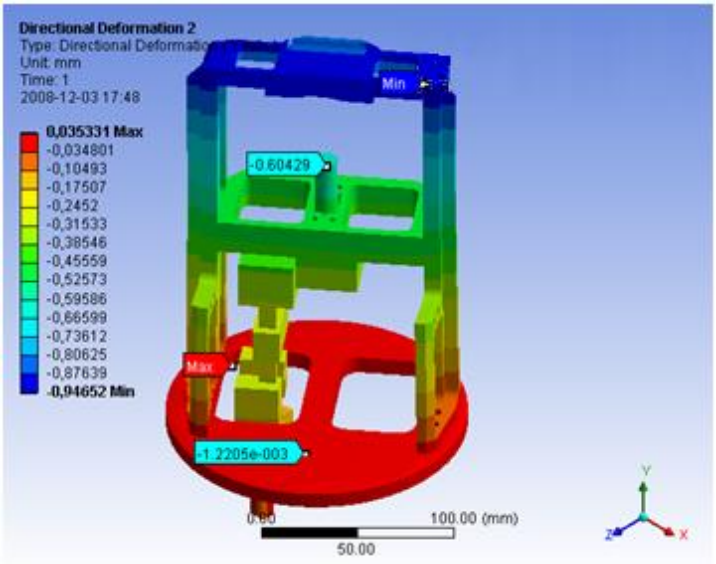

Figure 57. The Y-axis deformation of IF-chain at 4 K. The flag "-0.60429" is the deformation occurring at the top of the horn.

For minimizing the mechanical stress caused by thermal contraction of various materials, a titanium intermediate piece in the IF support bracket was introduced (Figure 58). This piece balances the difference of the contraction of aluminium parts as compared to the copper parts. The integral CTE values [28] for cooling from 300K to 4K for titanium ($1.7*10^{-3}$) can be compared to the values of copper ($3.3*10^{-3}$) and aluminium ($4.2*10^{-3}$). This shows that introducing of the titanium compensating piece allows matching of the thermal deformation of the optics support structure and IF chain. As a result, a rigid mechanical support of the IF chain has been designed, which meets requirements for the Eigen frequency (>70 Hz). Also the small titanium density (4.54 g/cm^3 value) helped fulfilling the strict mass budget of 2 kg at cold stages.

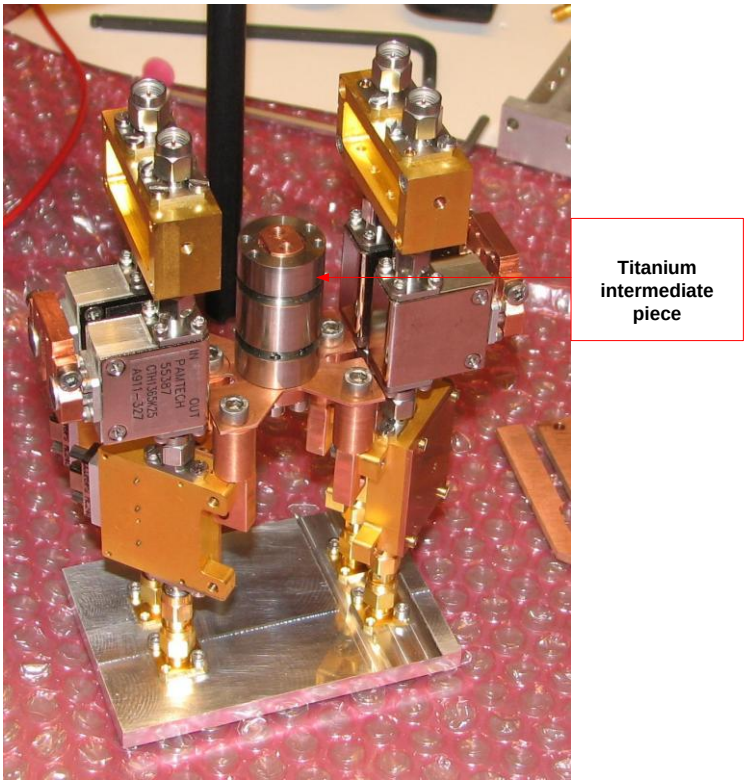

Figure 58. The titanium compensating piece in the IF support bracket together with components of the IF chains.

4.3. Thermal Deformation

4.3.1. Cartridge Study

During the cooling down from 300 to 4 Kelvin, the cartridge experiences thermal contraction and consequent stress due to the difference in thermal expansion coefficients of the materials used inside the cartridge as represented in Figure 59.

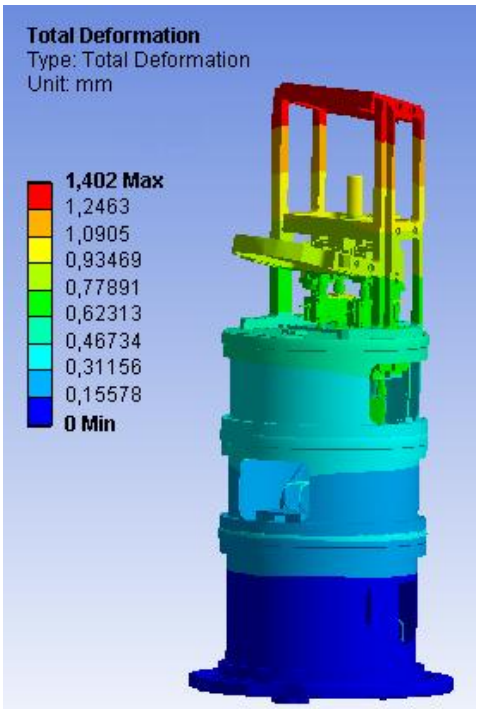

Figure 59. Total deformation of B5CCA.

The analysis using ANSYS gives the cartridge body deformation of 0.660 mm, measured as displacement of the 4K plate in respect to the 300K plate as a reference. Including thermal deformation of the optics, total Band 5 cartridge linear contraction is 1.402 mm and is quite consistent with the analytically (with simplification assumptions on the analyzed geometry) calculated value of 1.408 mm.

4.3.2. Thermal Deformation of the Optics Structure

Our studies of the Band 5 optics behaviour during cooling include, besides supporting structure, the optics interface to the 4 K cartridge plate comprising the screw joint and the guiding (dowel) pins of Ø1.5 and Ø4 mm as shown in Figure 60.

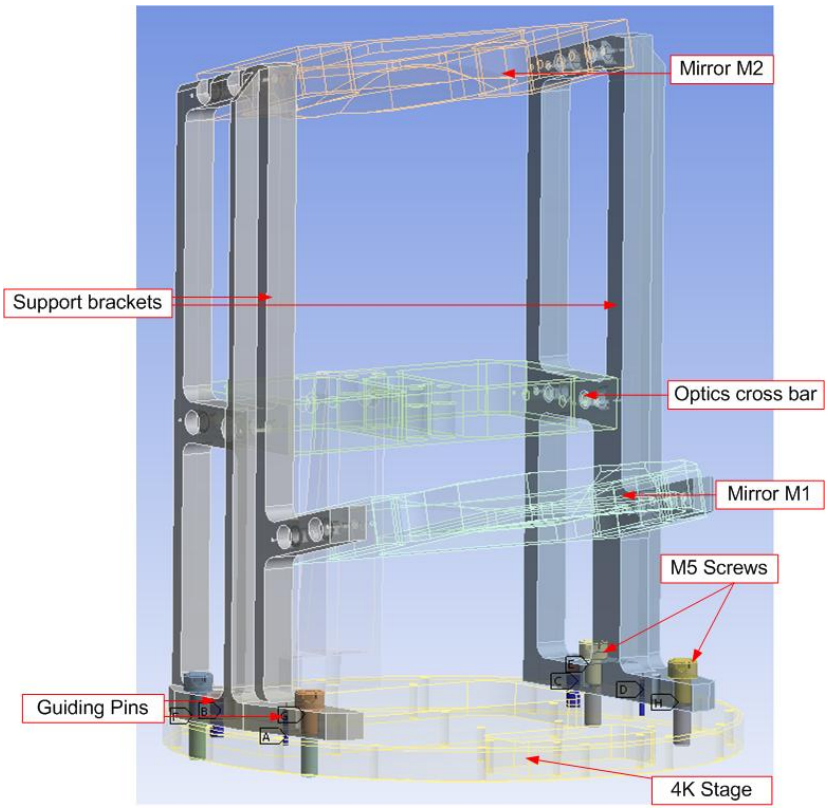

Figure 60. The optics structure with guiding pins and M5 screws attached to the 4K plate.

The materials of the components of the Band 5 optics are shown in TABLE 8 details on the optics design could be found in the reference [47].

TABLE 8 COMPONENTS OF THE BAND 5 OPTICS AT 4K PLATE

Element	**4K Plate**	**Optics structure**	**Screws and pins**
Material	Copper OFHC	Aluminium alloy EN5083 ALCA5	Stainless Steel

The motivation for the detail investigation was to prove that the screws and the pins could keep the optics structure at the reference location with respect to the optical design reference at the cartridge 4 K stage plate. The idea was to use the guiding pin of a bigger dimension (Ø4 mm) to provide a reference position of the optics structure at certain points of the 4 K plate as shown in Figure 61. While the pin with a smaller diameter of 1.5 mm assisted accurate placing of the vertical optics support brackets during the assembly.

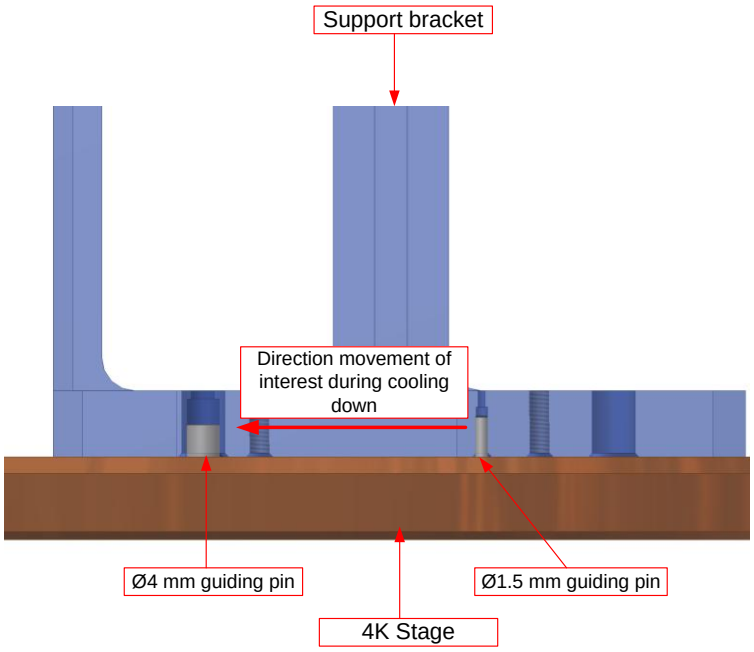

Figure 61. The placement of the guiding pins of the optics support brackets.

The investigation of the displacement is made with respect to the reference line in the X-axis (Figure 62).

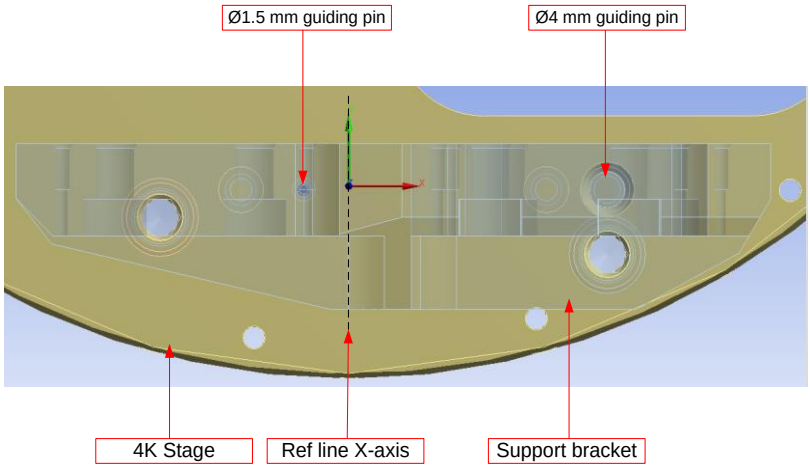

Figure 62. View above of an optic support bracket with reference line.

During cooling down, the deformation loads will apply mainly at the 1.5 mm pins due to its less rigidity than the 4 mm pins (Figure 63). The obtained deformation values of the optics structure (copper plate and aluminium support bracket) correspond to the calculated tolerances and provide support to the implemented design of using a bigger pin to provide the optics reference position.

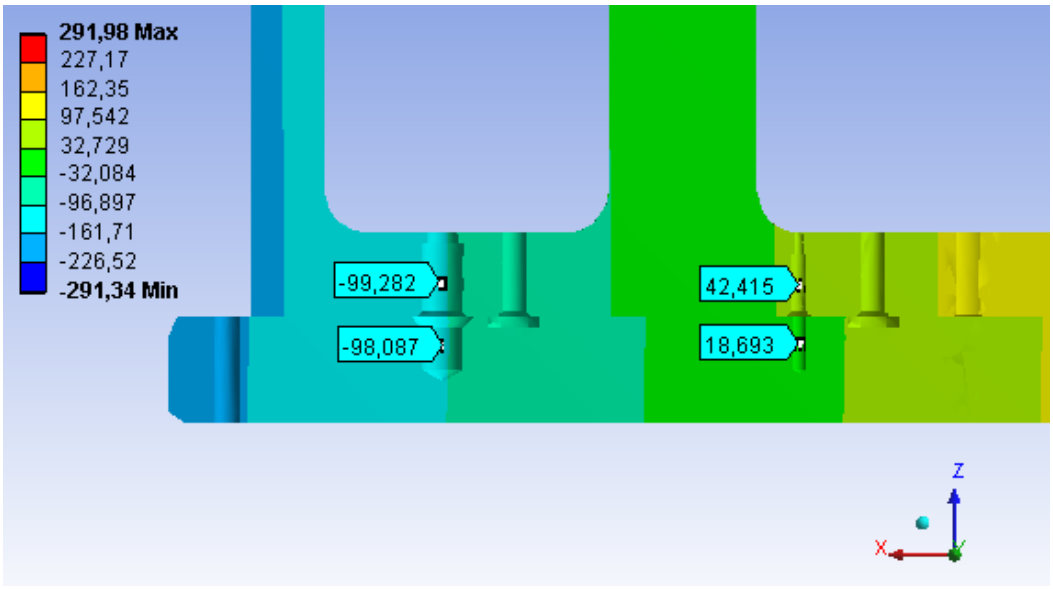

Figure 63. Deformation of optics structure in X-direction. The flag values (deformation) are in µm and in relation to a zero reference line. The Ø4 mm pin is marked with flags "-99.282" (support bracket) and "-98.087" (4K plate) while the Ø1.5 mm pin is marked with flags "42.415" (support bracket) and "18.693" (4K plate).

Figure 64 shows the obtained result of the parallel displacement of the optics structure with a maximum of 0.8 mm vertically and 0.3 mm in the direction parallel to the 4K plate.

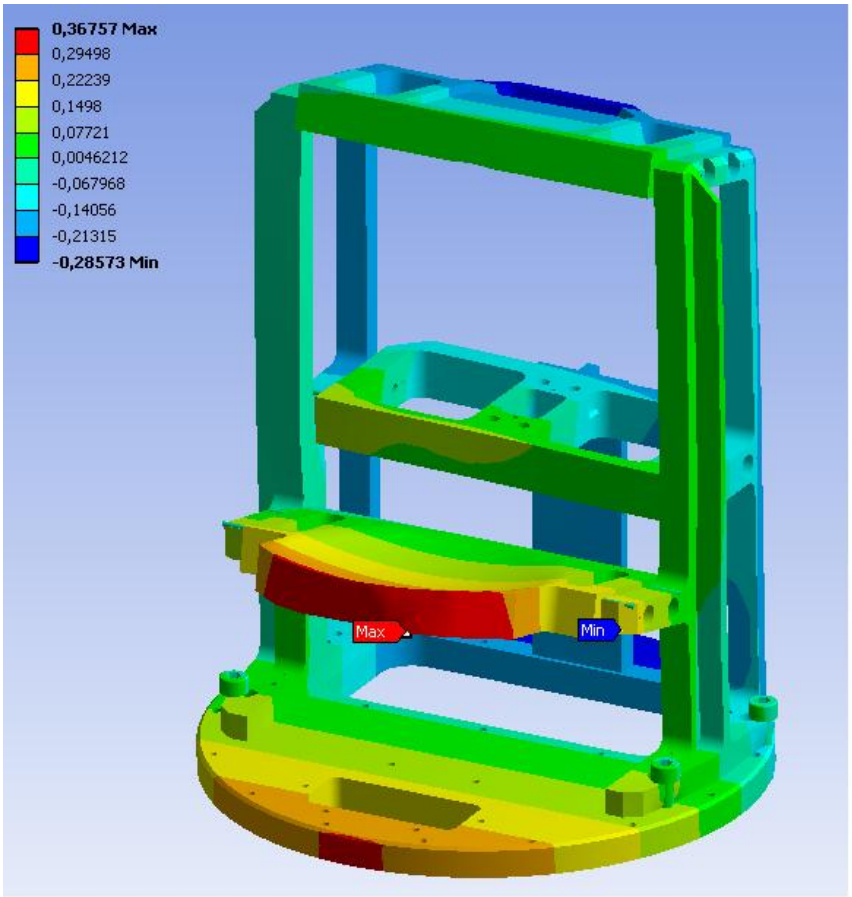

Figure 64. Thermal displacement of the optics structure as a result of cooling to 4 K.

As mention in section *4.1.1.3 Optical Specification and Tolerance Budget*, the optical specification shall have an aperture efficiency factor over 80%. The efficiency has been verified by measurement of the beam as reported in [66]. This is an experimental verification of the conclusions based on ANSYS simulation.

4.3.3. Thermal Deformation of the M5 Screws

Oversized M5 screws were used to attach the optics to the 4K plate. The analysis of the thermal deformations of the M5 screws was conducted to determine if an impact of the structure caused by the deformation should be considered.

Between the M5 screws joints at the ALMA band 5 optics structures and the interfacing 4 K plate stress and deformation are occurring. Interfacing parts are made of the following materials: copper for the 4 K plate, screws of stainless steel and the optics structure of aluminium alloy. The screws preload (bolt pre-tension) makes both the 4 K plate and optics structure experiencing deformation.
The preload was obtained by (4.7) [67]

$$F_i = \frac{T}{KD} \tag{4.7}$$

where T is the bolt installation torque, K is the torque coefficient and D is the bolt nominal size.

The K value is calculated by the following formula;

$$K = \frac{\left[\frac{0.5p}{\pi} + \frac{[0.5\mu_t(D - 0.75p\sin(\alpha))]}{\sin(\alpha)} + 0.625\mu_c D\right]}{D} \tag{4.8}$$

where p is the thread pitch (bolt longitudinal distance per thread),
α is the thread profile angle = 60° (for M, MJ, UN, UNR, and UNJ thread profiles).
B is the thread profile half angle = 60°/2 = 30°.
μ_t is the thread coefficient of friction.
μ_c is the collar coefficient of friction.

Figure 65 shows the screw deformation that affects the ALMA band 5 optics structure.

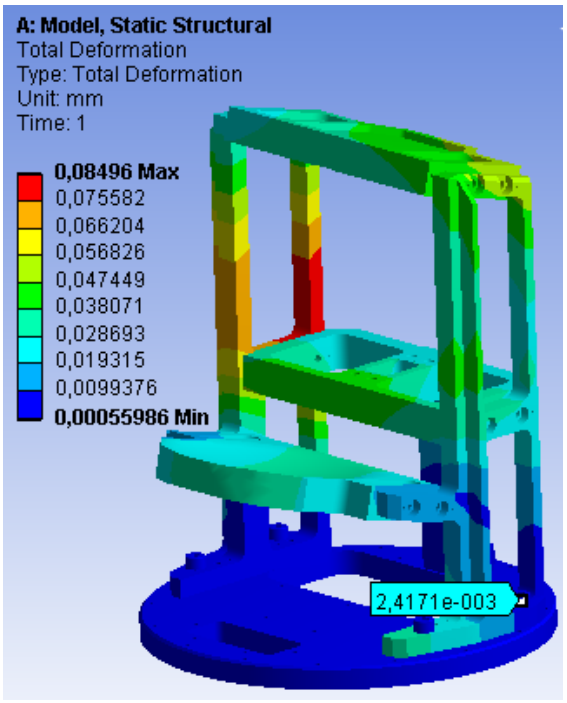

Figure 65. Screw deformation occurring at the optics structure. The deformation is marked with flag "2.4171e-003".

The analysis of the deformations gave values of few micrometers for all the screws and this contribution was neglected for further calculations.

4.4. Radiation Thermal Load

The installed optics in the cartridge does affect the radiation load that comes from the window to the 4 K stage. A blank cartridge model is used at 4 K stage with a flat copper flange. The optics and the receiver structure redistribute the IR illumination, partly scattered, and partly concentrating it at the area around the horn aperture. To verify any possible influence onto the 4 K stage of thermal load, the worse case was assumed – that the mirror is working as a black body

The Band 5 optics structure have experiences additional thermal load due to radiation, as compared to a blank cartridge, from the 300 K windows; a simplified model was used to estimate the additional load (Figure 66).

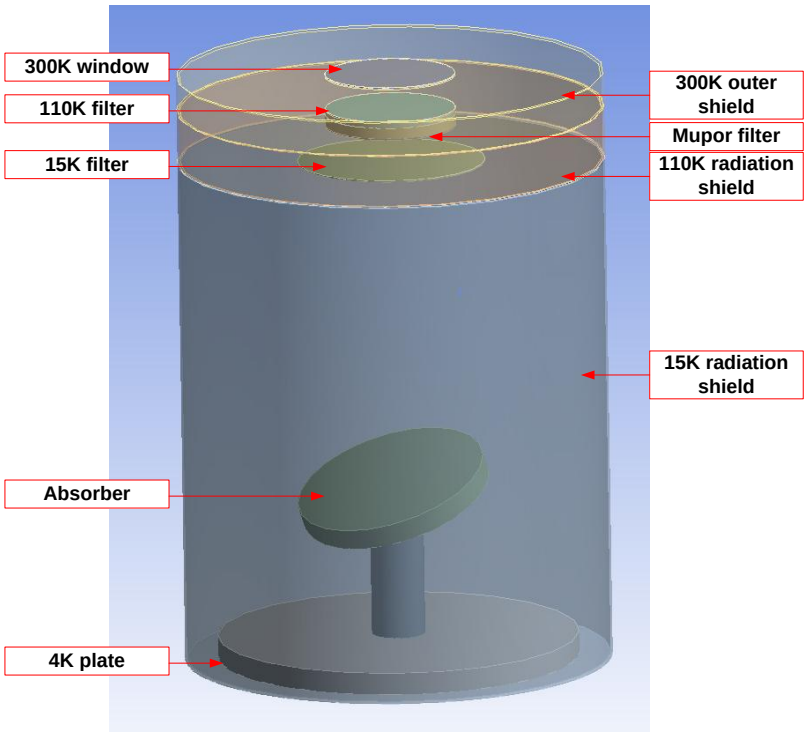

Figure 66. Model of B5CCA optics structure with 15K, 110K and 300K radiation shield. The radiation path from the 300K windows goes through the 110K filter, the Mupor© filter and the 15K filter.

The model is based on geometry of the cartridge test cryostat manufactured by NAOJ/NINS [68] (size and length between the radiation shields). The materials of the elements used in the model are shown in TABLE 9.

TABLE 9 COMPONENTS OF THE RADIATION MODEL OF BAND 5 OPTICS

Element	**4 K Plate**	**15 K, 110 K radiation shields**	**300 K outer shields**	**15 K, 110 K filter**	**Mupor filter**
Material	Copper OFHC	Ni-plated copper	Stainless Steel	Molded-PFA	Mupor

According to reference [69], the calculated IR load at the 4 K plate is in a range of 18 mW to 55 mW depending on optical design. Simulation shows that for the Band 5 optic layout, the total power that is radiated by the radiation filter in the assumption that 4K plate is acting as a black body, is 26 mW. For the simulation of the influence of the illumination optics, the 15K shield emissivity was assumed equal to 0.5, which allows us taking into account the view – factor for the decreasing model size and simulation time. Results of the simulations are shown in the TABLE 10. The results represent the total thermal load for the empty gold-plated 4 K plate (Case 1) and equipped with the optical system (Case 2).

TABLE 10 THE CASES FOR THE RADIATION MODEL OF BAND 5 OPTICS

Case 1	**Emissivity**	**Radiation load (mW) @ 4 K plate**
4 K plate	0.05	0.30
15 K radiation shield	0.5	
Case 2	**Emissivity**	**Radiation load (mW) @ 4 K plate**
4 K plate	0.05	2.70
15 K radiation shield	0.5	
Absorber	1	

Simulations show the obvious influence for the installation of the thermal load, which should be taking into account for proper thermal load calculations.

Further investigations were conducted with a full assembled optics structure with mirrors M1, M2 (emissivity of 0.05 as polished aluminium), support brackets and the horn. The results of the analysis of both the simplified one and the full optics model are presented in TABLE 11

TABLE 11 RESULTS OF THE POWER FOR BOTH ANALYSIS WITH THE SIMPLIFIED AND THE FULL OPTICS PATH

Component	**Absorber**		**4 K Plate**		**Mirror1**		**Mirror2**	
Model	**Simplified**	**Full**	**Simplified**	**Full**	**Simplified**	**Full**	**Simplified**	**Full**
Power (mW)	19	0.23	1.36	1.17	N/A	0.69	N/A	0.50

For the simplified model the absorber picks up the radiation load of 19 mW when the radiation comes from the 300 K window and going through various IR filters while the 4 K plate absorbs 1.36 mW. This gives a total value of the 4 K stage thermal load of 20.36 mW. This can be compared with the full optics path model where the absorber only picks up 0.23 mW and the 4 K plate absorbs 1.17 mW.

The temperatures at the 110 K, 15 K and the mupor filter decreased with the full optics (TABLE 12).

TABLE 12 RESULTS OF THE TEMPERATURE FOR BOTH ANALYSIS WITH THE SIMPLIFIED AND THE FULL OPTICS PATH

Component	**Absorber**		**15 K filter**		**Mupor filter**		**110 K filter**	
Model	**Simplified**	**Full**	**Simplified**	**Full**	**Simplified**	**Full**	**Simplified**	**Full**
Temperature (K)	4.4	4.1	135	83	177	144	220	195

The difference between the cases is the simplified case has a large copper block between the absorber and the 4 K plate while the full optics has a cooling path from the 4 K plate of aluminium (optics supports) and copper (horn).

4.5. Mechanical Design

The following specification requirements have been verified by simulation: added mass should be not more than 2 kg; Eigen frequency of the construction elements of the cartridge

should be above 70 Hz; cabling should not break due to thermal stress; finally, alignment tolerances and optics performance should be preserved for tilting the cartridge up to 90 degrees. This section will go through some of the analysis that was carried out.

4.5.1. Vibration

The vibration issue is important in a view of transportation of a telescope to and at the high-mountain site, as well as during normal operation of the cartridge in the telescope with very fast moving of the antenna. The specification [61] of the cartridge puts the first Eigen frequency at least at 70 Hz or greater. By using the ANSYS software, the vibration modal analysis was performed on the Band 5 cartridge 3D model. Simulation uses corrected value for the elastic modulus for the G10 material, 10.9 GPa, which have been verified experimentally for the similar construction part [70]. Interestingly, it was reported by NOVA (Band 9) a discrepancy concerning the stiffness value of the G10 fibreglass spacers of the cartridge body [70]. To resolve this issue a deflection measurement was performed that ended up with a conclusion that the Elastic Modulus of 35 GPa of the fibreglass has to be reduced down to 10.9 GPa. As a result, the structure of the cartridge with the optics has its first frequency at 123.4 Hz and when the table value for the fibreglass stiffness is used and with the new corrected stiffness becomes 82.2 Hz, which introduces a major change in the Eigen frequencies but still fulfils the specification of 70 Hz. The greatest vibration amplitude occurs in the Y-direction.

4.5.2. Magnetic Flux Analysis

Band 5 is using non-superconducting coils for suppression of Josephson current in the SIS mixer. The coils are placed at the top of the B5CCA mixer block and the magnetic flux is lead by iron magnetic concentrators to the mixer junctions as depicted in Figure 67. The normal coils, employing Cu wire of about Ø0.06 mm, are used because of the space constrains.

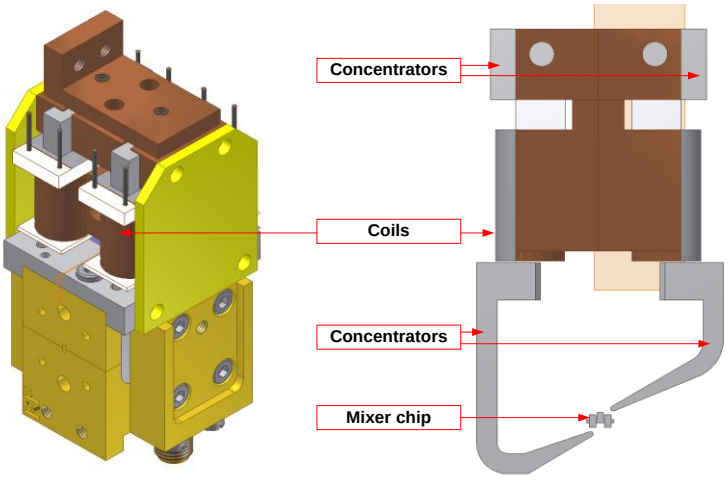

Figure 67. To the left, a 3D model of the B5CCA mixer block. To the right, a cut through the mixer block with coils, concentrators and mixer.

As described in the chapter 2, a SIS junction does have in addition to the quasiparticle current, a cooper pair current also known as Josephson current. When an LO signal is

introduced large Shapiro steps are appearing and causes instability and additional noise to the mixer. To keep stable operation of the junction mixer, a suppression of the *Josephson current* must be conducted [12].
When a magnetic field is applied the phase difference (δ) of the Copper pairs (θ_1, θ_2), $\delta = \theta_1 - \theta_2$ is no longer constant, it varies with the magnetic field according to,

$$\frac{\partial \delta}{\partial t} = \frac{2\pi}{\Phi_0}\Phi \tag{4.9}$$

where Φ is the magnetic flux and Φ_0 is the magnetic flux quantum

$$\Phi_0 = \frac{h}{2e} \tag{4.10}$$

where h is Planck's constant and e is elementary charge.

The magnetic field perpendicular to the current through the junction will modulate the critical current,

$$I_0(\Phi) = I_0(0)\left|\frac{\sin(\pi\frac{\Phi}{\Phi_0})}{\pi\frac{\Phi}{\Phi_0}}\right| \tag{4.11}$$

With excessive magnetic flux applied the function $\mathrm{Sin}(\Phi)/\Phi_0$ relaxes to nearly zero Josephson current.

The normal coils produce heat, which is isolated from the mixer block by placing the entire coil assembly suspended over the 2SB mixer block and providing thermal isolation by fibreglass parts (yellow vertical support panels, Figure 67); in order to avoid heat sinking into the mixer block via the magnetic concentrators a gap is introduced, Figure 68.

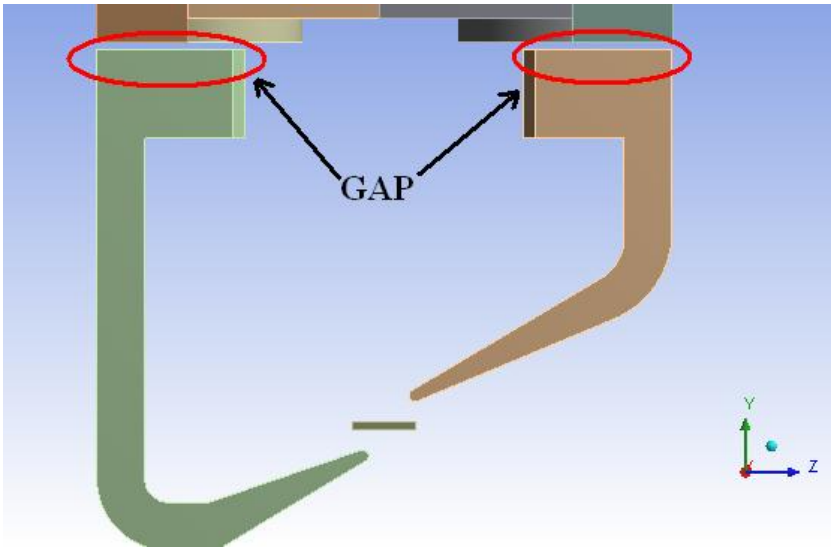

Figure 68. The gap is located between the coils and the iron concentrators.

The gap increases magnetic resistance of the magnetic circuit and precludes saturation of the magnetic concentrators but leads to the increasing of the coil current and that produces additional power dissipation. The optimum gap size is one of the factors considered during simulations together with different currents (1, 3, 6 mA) running through the coils with a resistance of one coil of about 200 Ω.

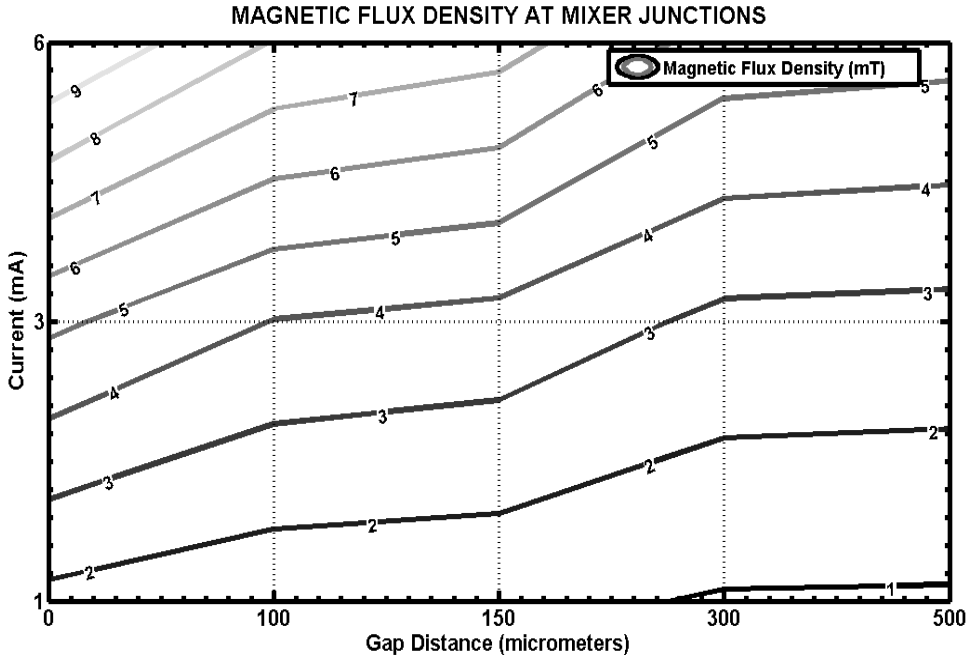

Figure 69. The magnetic flux density presented in a contour plot with various current values and gap distance with discrete values.

In order to keep the magnetic flux loss at the gap at an acceptable level, while maintaining reasonable thermal insulation the gap between the magnetic concentrators must be optimize between these two contradictory requirements. Additionally, the manufacturing tolerance was accounted when the gap distance was chosen to 150 μm (Figure 69). The optimization did bring down the coils power consumption from 7.2 mW to 1.6 mW [71].

The copper thermal link from the 4 K plate to the mixer does affect the temperature distribution that occurs at the mixer junctions. Figure 70 presents a plot of the temperature of the junctions based on various power dissipations of a coil (0.2, 1.8, 7.2 mW) and different lengths of the copper wire thermal link.

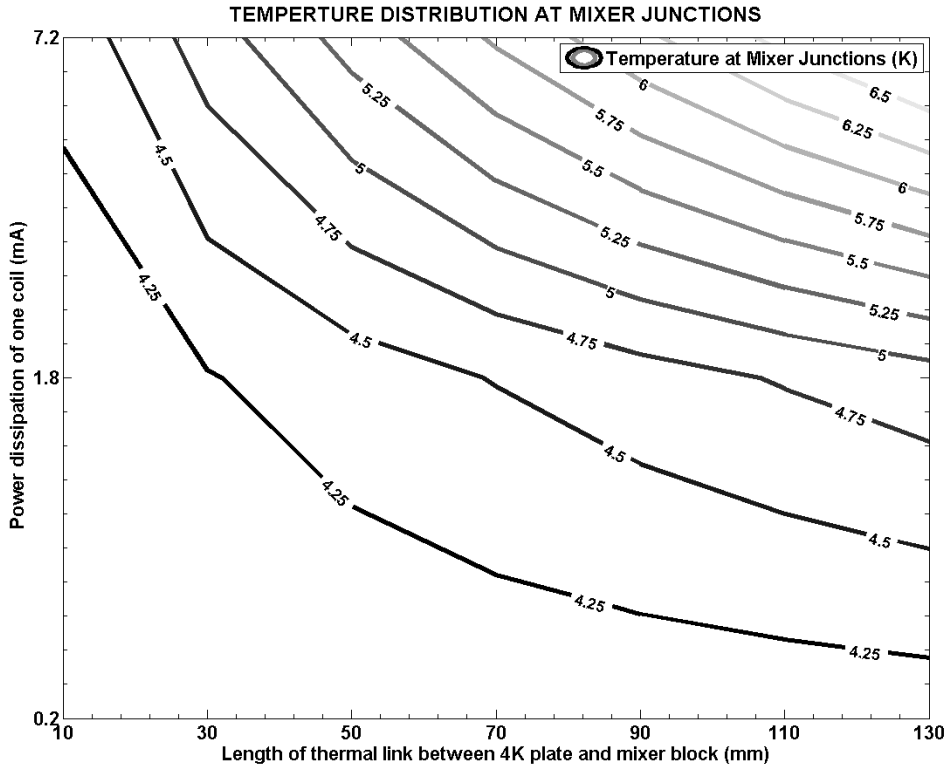

Figure 70. The temperature distribution that is present at the mixer junctions with parameters of the thermal link length between 4K plate and mixer block, and the power dissipation of a coil.

4.5.3. Stress Analysis

To relief stress occurring at the IF-cables and the waveguides during a cooling down, the design for their path must be made to avoid excessive mechanical stress. In order to allow flexibility and stress releaf we used bended traces; the bends radius of the waveguides is 20 mm, while the coaxial cables bend is 7 mm of radius and this defined by RF requirements.

The obtained results for the equivalent stress are shown in Figure 71. The stress analysis of the waveguides was of the concern, because of up to 0.4 mm deformation due to the difference between thermal contraction of the cartridge body and the waveguides [49], so a corresponding load of the difference (1 N) was applied. The maximum equivalent stress was determined to be 27 MPa, which is far below the yield stress of 240 MPa of stainless steel 304.

Figure 71. The equivalent stress (von-Mises) for the waveguides.

For the IF-cables the differential contraction between the cartridge and the IF-cables is around 0.1 mm so the equivalent stress is found to be 6.8 MPa.

4.5.4. Deformation Due to Gravity

The deformations due to the gravity were investigated for two cases, namely in X-direction and Z-direction. The X-direction is corresponding to antenna position of 90 degrees about the elevation axis, while Z-direction is 0 degrees about the elevation axis.

The deflection of the cartridge in the X-directional is 0.75 micrometer while at the optics support, the mirror M1 gives a deformation of 2.29 micrometer. These values are insignificant and prove sufficient stiffness of the B5CCA.

For the deformation in Y-direction, the cartridge structure show a result of 19.4 micrometer and the mirror M2 at the optics support has a result of 27.4 micrometer as shown in Figure 72.

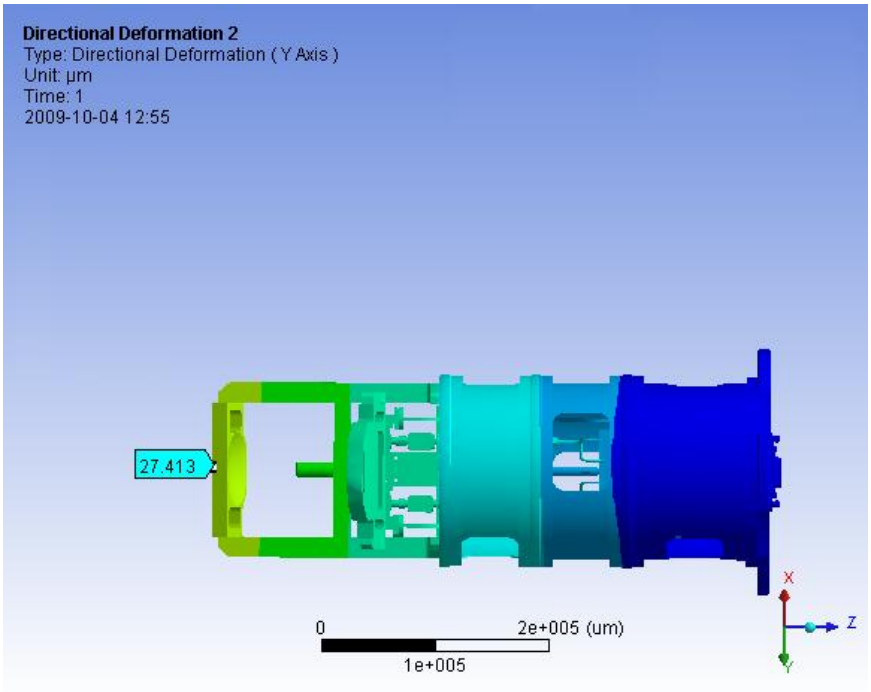

Figure 72. Cartridge and optics support deformation due to gravity in Y-direction with a maximum deflection amplitude marked point "27.413".

Given that there are uncertainties in the temperature distribution in the cartridge in the Z-direction along the fibreglass joints of the cold plates and the base plate, the mechanical parameters for the cartridge body was defined at room temperature. Bearing in mind that stiffness increases in nearly all materials during cooling, the result of the simulations can be considered as a pessimistic approximation.

Chapter 5

Conclusion

This licentiate thesis has discussed different aspects of the thermo-mechanical analysis of the ALMA Band 5 Cold Cartridge Assembly design and its optimization for operation at (cryogenic) working conditions.

The work of the author for the optimization part has been focused on the design of internal cabling and heat sinks to achieve the optimum the thermal heat load at temperature stages; 110 K, 15 K and 4 K. By presenting an optimization procedure for the DC wiring length and showing the complexity of the thermal load due to conductivity and resistivity, a modeling was conducted for estimating the dissipated power between 15 K and 4 K stages for various currents and lengths. The design issue with the development of the heat sinks throughout the prototyping of the B5CCA was dealing with concerns such as providing a good thermal link for reducing the thermal influx through cables and avoid thermal stress that would occur during cooling down from room temperature to cryogenic temperature.

The design issue of the long IF chain presented in the thesis regards to the thermal contraction during cooling that could develop dangerous mechanical stress, which may cause damaging of certain components of the IF chain. This solved by introducing a titanium intermediate piece in the IF support bracket that allowed matching of the thermal deformation of the optics support structure and the IF chain. This resulted in a more rigid mechanical support of the IF chain, meeting Eigen frequency specification of 70 Hz

By investigation of the thermal deformation of the full cartridge and the optics structure, the behaviour of the Band 5 optics during cooling and how it can affect the illumination efficiency were carried out. The idea for the investigation was to prove that the screws and the pins could keep the optics structure at the reference location with respect to the optical design reference at the cartridge 4 K stage plate. By the usage of a guiding pin of a bigger dimension (Ø4 mm), a reference position of the optics structure at certain points of the 4 K plate was provided, while the pin with a smaller dimension (Ø1.5 mm) aid with accurate placing of the vertical optics support brackets during the assembly. The obtained information from analytical calculations and simulations show support to the implemented design of using a bigger pin to provide the optics reference position

The IR radiation load that comes from the window to the 4 K stage is affected by the optics structure in the cartridge and during investigation the worse case was assumed, namely that the mirror was working as a black body. By the usage of two different models, one simplified with only 4 K stage with a flat copper flange, radiation shields and absorber, and one complete with the full optics structure, radiation shields and absorber, the illumination optics path are shown given additional thermal load values of 4 K plate in the region of 1 mW.

With analysis of vibration, cartridge tilting and stress in the internal cabling, the mechanical design are shown to verify specification requirements such as the added mass should be no more than 2 kg, Eigen frequency of the B5CCA above 70 Hz, no breakage of internal cabling and finally alignment tolerances and optics performance are shown to be achieved.

The magnetic flux analysis optimizes the magnetic circuitry employed for suppression of the Josephson current in SIS mixers and, as a result of the optimization, the power consumption was reduced from 7.2 mW to 1.6 mW.

So by conducting a thermo-mechanical analysis of the B5CCA assembly, the design is shown to be fulfilling all specifications for operation in the cryogenic operational environment.

Chapter 6

Summary and Discussion of Appended Papers

6.1. Summary and Discussions, Paper A

”Analysis, Simulation and Design of Cryogenic Systems for ALMA Band 5 Prototype Cartridge”

M. Strandberg, I. Lapkin, V. Belitsky, A. Pavolotsky, and S.-E. Ferm

Proceedings of the 20TH INTERNATIONAL SYMPOSIUM ON SPACE TERAHERTZ TECHNOLOGY, Charlottesville, VA, USA, April 20-22, 2009, s. 307-310

This paper presents analysis and simulation results for the thermal and mechanical design of the ALMA Band 5 cartridge that has been carried out using different FEM software packages such as CFDesign and ANSYS. By comparing simulation results obtained with these software and the analytical calculations ANSYS were shown to be give more accurate in comparison. This paper also presents mechanical design, where the major focus was put on the cartridge and the optics support structure deformation with cooling.

6.2. Summary and Discussions, Paper B

”Cryogenic, Mechanical Analysis and Simulation for ALMA Band 5 Prototype Cartridge”

M. Strandberg, I. Lapkin

Submitted to Instruments and Experimental Techniques (Pribory i Tekhnika Eksperimenta), 2011

This paper presents procedure of thermal-mechanical modelling performed partly analytically and with the FEM software package ANSYS for the B5CCA. A DC wiring length optimization procedure is included and a discussion about the complex thermal load due to conductivity and resistivity in cryogenic wires. The paper present also simulations for the thermal deformations of the B5CCA and the optics structure which confirms the usage of a bigger guiding pin and smaller pins for providing support for the optics reference position. For minimizing mechanical stress caused by thermal contraction in the IF chain, analysis were conducted which lead to a titanium intermediate piece in the IF support bracket was introduced. The mechanical design spotlights vibration analysis (Eigen frequency) for contraction elements of the cartridge and magnetic flux analysis where optimizing of gap distance between Josephson suppression current coils and iron concentrators was the main task.

List of Abbreviations

2SB	Side Band Separation
ALMA	Atacama Large Millimeter Array
APEX	Atacama Pathfinder Experiment
B5CCA	ALMA Band 5 cartridge Assembly
CAD	Computer-aided Design
CTE	Coefficient of Thermal Expansion
DC	Direct Current
EMI	Electromagnetic Interference
ESD	Electrostatic Discharge
FEM	Finite Element Method
GaAs	Gallium Arsenide
GARD	Group for Advanced Receiver Development
HEMT	High Electron Mobility Transistor
HIA	Herzberg Institute of Astrophysics
IF	Intermediate Frequency
InP	Indium Phosphide
IRAM	Institut de Radioastronomie Millimétrique
LNA	Low Noise Amplifier
LO	Local Oscillator
NAOJ	*National Astronomical Observatory of Japan*
NINS	*National Institutes of Natural Sciences*
NOVA	Netherlands Research School for Astronomy
NRAO	*National Radio Astronomy Observatory*
OFHC	Oxygenfree, High-conductivity
OMT	Orthomode Transducer
OSO	Onsala Space Observatory
PCB	Printed Circuit Board
PTFE	Polytetrafluoroethylene
PWV	Perceptual Water Vapor
RF	Radio Frequency
RRR	Residual Resistivy Ratio
SIS	Superconductor Insulator Superconductor
SSB	Single Side Band
TeCu	Tellurium copper
WCA	Warm Cartridge Assembly

References

Disclamer: The *-marked references are not available publicity. For gain access please contact administrators for ALMA Project documentation server.

1. K. G. Jansky, *Electrical Disturbances Apparently of Extraterrestrial Origin.* Proceedings of the IRE, 1933. **21**(10): p. 1387-1398.
2. http://www.ssc.se/?id=7180.
3. http://sci.esa.int/herschel/.
4. http://www.apex-telescope.org/.
5. http://www.almaobservatory.org/.
6. H. Rudolf, M. Carter, and A. Baryshev, *The ALMA Front End Optics - System Aspects and European Measurement Results.* Antennas and Propagation, IEEE Transactions on, 2007. **55**(11): p. 2966-2973.
7. G.A.Ediss, *Cryostat heat loads and achieved Temperatures - FEND-40.03.00.00-071-D-REP*. available from ALMA Project documentation server., 2007.
8. A. Orlowska, *ALMA Cartridge Assembly Procedure - FEND-40.03.00.00-073-D-PRO*. available from ALMA Project documentation server., 2008.
9. G. Beherens, et al., *Guidelines for the design of Cryogenic Systems*. National Radio Astronomy Observatory. Electronics Division. Internal report No 306, 1997.
10. J.R. Tucker, *Quantum limited detection in tunnel junction mixers.* IEEE J. of Quantum Electron, 1979. **QE-15**(11): p. 1234-1258.
11. J.R. Tucker and M.J. Feldman, *Review of Modern Physics.* Quantum Detection at Millimeter Wavelengths, 1985. **57(4)**: p. 1055-1113.
12. Charles. P. Poole. Jr., ed. *Handbook of superconductivity* 2000, Academics Press.
13. J.R. Waldram, *Superconductivity of Metals and Cuprates.* 1996, Bristol: Institute of Physics Publishing.
14. Klaus D. Timmerhaus and Richard P. Reed, ed. *CRYOGENIC ENGINEERING Fifty Years of Progress*. 2007, Springer Science+Business Media, LLC.
15. G. Perinić, G. Vandoni, and T. Niinikoski. *Introduction to Cryogenic Engineering*. 2005; Available from: www.slac.stanford.edu/econf/C0605091/present/CERN.PDF.
16. R.G. Scurlock, ed. *History and Origins of Cryogenics*. 1992, Clarendon Press: Oxford.
17. F. Din and A.H. Cockett, *Low-Temperture Techniqiues*. 1960, London and Tonbridge: Whitefriars Press LTD.
18. Guy K. White, *Experimental Techniques in Low-Tempeature Physics*. 3 ed. 1979, Oxford: Claredon Press.
19. Russel B. Scott, *Cryogenic Engineering*. 1959, Princeton: D. Van Nostrnad Company Inc.
20. John H. Lienhard IV and John H. Lienhard V, *A Heat Transfer Textbook*. 3 ed. 2008, Cambrige, MA: Phlogiston Press.
21. J. P. Holmen, *Heat Transfer*. 6 ed. 1986, New York: McGraw-Hill Book Co.
22. Björn Palm. *A Short Course on Heat Transfer*. 2007; Available from: http://www.energy.kth.se/courses/4A1602/2007/Lecture%20notes/heat%20transfer/HEAT%20TRANSFER4.pdf.
23. Vedat S. Arpaci, Shu-hsin Kao, and Ahmet Selamet, *Introduction To Heat Transfer*. 2000, Upper Saddle River, NJ: Prentice Hall.

24. Thomas M. Flynn, *Cryogenic Engineering*. 2 ed. 2005, New York: Marcel Dekker.
25. Michael Modest, *Radiative Heat Transfer*. 2 ed. 2003, San Diego: Academic Press.
26. R. J. Foley. *Topic 3.8: Thermal Stress, Strain & Deformation I*. Available from: http://www3.uwstout.edu/faculty/scotta/upload/Foley-StaticsStrengths.pdf.
27. Alexander Kynin, Seunglhee Suh, and Seungheon Han. *Thermal Deformations in Engineering*. in *TRIZCON2006*. April 2006. Milwaukee WI USA.
28. Cryogenic Technology Group at National Institute of Standards and Technology. Available from: http://cryogenics.nist.gov/.
29. Lake Shore Cryotronics Inc. Available from: http://www.lakeshore.com/.
30. ICE Oxford Ltd. Available from: http://www.iceoxford.com/.
31. Jack W. Ekin, *Experimental Techniques for Low-Temperature Measurements: Cryostat design, material properties and Superconductor Critical-Current Testing*. 2006: Oxford University Press.
32. R. Poggiani, *ET-026-09, Materials and components of possible interest for cryogenic operation of Einstein Telescope*. 29/10/2009, University of Pisa and INFN Pisa.
33. Adam L. Woodcraft and Adam Gray, *A low temperature thermal conductivity database.* AIP Conference Proceedings, 2009. **1185**(1): p. 681-684.
34. Adam L. Woodcraft, *Predicting the thermal conductivity of aluminium alloys in the cryogenic to room temperature range.* Cryogenics, 2005. **45**(6): p. 421-431.
35. Joseph Callaway, *Model for Lattice Thermal Conductivity at Low Temperatures.* Physical Review, 1959. **113**(4): p. 1046.
36. M. G. Holland, *Phonon Scattering in Semiconductors From Thermal Conductivity Studies.* Physical Review, 1964. **134**(2A): p. A471.
37. J.E. Jensen, et al., eds. *Summer study on superconducting devices and accelerators - selected cryogenic notebook*. 1980, BROOKHAVEN NATIONAL LABORATORY.
38. Y.A. Cengel and M.A Boles, *Thermodynamics: An Engineering Approach*. 5 ed. 2006, Boston: McGraw-Hill Higher Education.
39. R. J. Foley. *Stress, Strain & Hooke's Law - II*. Available from: http://www3.uwstout.edu/faculty/scotta/upload/Foley-StaticsStrengths.pdf.
40. ; Available from: http://www.upscale.utoronto.ca/IYearLab/WilberforceRefShear4of8.pdf.
41. S. Atallah, *A relationship between emissivity and thermal conductivity of metals.* British Journal of Applied Physics, 1966. **17**(4): p. 573.
42. V. Musilova, et al., *Low temperature radiative properties of materials used in cryogenics.* Cryogenics, 2005. **45**(8): p. 529-536.
43. R Keith Mobley, *Root Cause Failure Analysis* 1999, Oxford: Elsevier.
44. ANSYS simulation software from ANSYS Inc.; Available from: www.ansys.com.
45. ALMA Band 5 Cartridge Team. *ALMA Band 5 Cold Cartridge Assembly Design Report FEND-40.02.05.00-010-B-REP*. Available from: ALMA Project documentation server.
46. V. Belitsky, et al. *Design and performance of ALMA band 5 receiver cartridge*. in *35th International Conference on Infrared Millimeter and Terahertz Waves (IRMMW-THz),* . Sept. 5-10 2010.
47. V. Belitsky, et al. *Prototype ALMA Band 5 Cartridge: Design and Performance*. in *Proceedings of the 20th International Symposium on Space Terahertz Technology*. April 20-22, 2009. Charlottesville.
48. *Cryostat Technical Specifications-FEND-40.03.00.00-002-B-SPE*. Available from: ALMA Project documentation server.

49. M. Strandberg, et al. *Simulation and Design of Cryogenic Systems for ALMA Band 5 Prototype Cartridge*. in *Proceedings of the 20th International Symposium on Space Terahertz Technology*. April 20-22, 2009. Charlottesville.
50. M. Carter, et al. *ALMA Front-end Optics Design Report - FEND-40.02.00.00-035-B-REP*. Available from: ALMA Project documentation server.
51. M. Whale, et al. *Physical Optics Analysis of the ALMA Band 5 Front End Optics*. in *Proceedings of the 19th International Symposium on Space Terahertz Technology*. April 28-30, 2008. Groningen.
52. 3D EM Field simulation software from Computer Simulation Technology AG.; Available from: www.cst.com.
53. Bhushan Billade, *Design of Dual Polarization Sideband Separation Mixer for ALMA Band 5, Thesis for the degree of licentiate of engineering*, in *Deparement of Radio and Space Science*. 2009, Chalmers University of Technology: Göteborg.
54. ALMA Band 9 Cartridge Team. *ALMA Band 9 Cartridge Critical Design Review Design Report FEND-40.02.09.00-078-A5-REP*. Available from: ALMA Project documentation server.
55. Erik Sundin, *Development of Cryogenic Low Noise 4-8 GHz HEMT Amplifier and its Advanced Characterization, Thesis for the degree of licentiate of engineering*, in *Deparement of Radio and Space Science*. 2006, Chalmers University of Technology: Göteborg.
56. Micro-Coax web-site. Available from: http://www.micro-coax.com/.
57. SSI Cable Corp.; Available from: http://www.ssicable.com/.
58. A.-L. Fontana and B. Lazareff, *Mode conversion and Resonant Absorption in Bent Overmoded Waveguides.* ALMA memo 550, 2006.
59. Aerowave Inc. Available from: http://www.aerowave.net/.
60. *ALMA Front End Thermal Budget-FEND-40.00.00.00-050-B-GEN*. Available from: ALMA Project documentation server.
61. *Band 5 Cartridge Technical Specifications-FEND-40.02.05.00-001-A-SPE*. Available from: ALMA Project documentation server.
62. *Front-End Sub-System for the 12 m-Antenna Array Technical Specifications-ALMA-40.00.00.00-001-A-SPE*. Available from: ALMA Project documentation server.
63. B. Lazareff, *Alignment tolerances for ALMA optics.* ALMA memo 395, 2007.
64. H.-M. Chang and M. J. Kim, *Optimization of conduction-cooled current leads with unsteady operating current.* Cryogenics, 2009. **49**(5): p. 210-216.
65. Cryoconnect -Tekdata. Available from: http://www.cryoconnect.com/.
66. *Band 5 Cold Cartridge Assembly Test Report – FEND-40-02.05.00-050-A-REP*. Available from: ALMA Project documentation server.
67. Garrett D. Euler. *Bolt Preload Calculation*. Available from: http://euler9.tripod.com/fasteners/preload.html.
68. Y. Sekimoto, et al., *Cartridge Test Cryostats for ALMA Front End.* ALMA memo 455 2003.
69. W. Grammer, et al., *Proposal for ALMA Front End Optics.* ALMA memo 324, 2000.
70. *ALMA Band 9 Cartridge Pre-Production Design Verification Test and Analysis Result - FEND-40.02.09.00-291-A2-REP*. Available from: ALMA Project documentation server.
71. Tech lic. B. Billade, GARD, private communication.

Paper A

Analysis, Simulation and Design of Cryogenic Systems for ALMA Band 5 Prototype Cartridge

M. Strandberg, I. Lapkin, V. Belitsky, A. Pavolotsky, and S.-E. Ferm

Proceedings of the 20TH INTERNATIONAL SYMPOSIUM ON SPACE TERAHERTZ TECHNOLOGY, Charlottesville, VA, USA, April 20-22, 2009, s. 307-310

Paper B

Cryogenic, Mechanical Analysis and Simulation for ALMA Band 5 Prototype Cartridge

M. Strandberg, I. Lapkin

Submitted to Instruments and Experimental Techniques (Pribory i Tekhnika Eksperimenta), 2011